Master's Thesis

Master's Degree in Nuclear Engineering

Implementation of dynamic nuclear fuel thermo-mechanics in transient simulation of lead-cooled reactors

Pau Aragón Grabiel

January 18, 2021

Supervisor: Janne Wallenius

Examiner: Lluis Batet Miracle

Call: January 2021

Barcelona School of Industrial Engineering

Abstract

The nuclear industry must address the issues faced by the current new-built plants in the western world if it is to remain cost-competitive with other forms of electricity generation. Serial, factory-based production of small modular reactors may address all of these issues. In this context enters SEALER, a lead-cooled fast reactor designed in the most compact configuration possible for commercial power production in off-grid areas.

Lead Cold and KTH Royal Institute of Technology are developing a multi-point dynamics code (BELLA) intended for use in the safety-informed conceptual design of lead-cooled fast reactors. Its development is motivated by relatively restricted options to apply modifications to currently available system codes. This master's thesis aims to improve the accuracy of BELLA by implementing a module for simulation of nuclear fuel thermo-mechanical performance, including the effects of thermal expansion of the fuel and cladding, fission gas release, and swelling of the fuel. Moreover, it constitutes a comprehensive review of the reference code.

The thermal expansion of the fuel pellet and cladding are estimated from temperature variations and their respective thermal expansion coefficients. An analytical expression for the thermal conductivity of irradiated UO_2 fuel is formulated considering the effects of porosity, solid fission products (precipitated and dissolved), and radiation damage. Fission gas release into the fuel-cladding gap is determined by assuming a total release above a burnup-dependent temperature threshold (Vitanza threshold) and a release-to-birth ratio of 1% otherwise. Gaseous swelling of the fuel is calculated from the density of the oxide pellet, which is described by a linear function of burnup. Solid-to-solid heat conduction between the fuel and the cladding is implemented, thus providing the possibility to simulate gap closure.

The performance of SEALER under unprotected transient overpower conditions is examined using BELLA with and without the fuel thermo-mechanics extension. The results indicate that the fuel centreline temperature is underestimated by the reference code. Nevertheless, the safety margin to fuel melting is still significant. Conversely, the fuel outer temperature is overestimated. There are two reasons for this, depending on the level of burnup. At the beginning of life, the thickness of the gap decreases due to the thermal expansion of the fuel, thereby enhancing heat transfer from the fuel to the cladding. On the other hand, as burnup increases beyond 3% gap closure occurs, and improved heat conduction results from direct solid-to-solid contact.

Contents

Nomenclature

Symbols

α Coefficient of thermal expansion

α_{axial} Axial expansion reactivity feedback

α_{Pb} Coolant temperature reactivity feedback

α_{radial} Radial expansion reactivity feedback

β_j Decay heat power fraction

β_{eff} Total effective delayed neutron fraction

β_i Effective delayed neutron fraction

χ Atomic fraction

ΔP_{fr} Frictional pressure drop

ΔP_{HS} Hydrostatic pressure difference

ΔP_{pump} Pump-head

δ_c Cladding thickness

$\dot{B}_{\text{Xe}}$ Xenon atoms birth rate

$\dot{m}$ Mass flow rate

$\dot{Q}$ Fission power

$\dot{Q}(0)$ Steady-state fission power

$\dot{Q}_b$ Helium gap conductance term

$\dot{Q}_{rad}$ Fuel-cladding radiation term

γ Pore shape factor

κ_P Porosity factor

κ_{DFP} Dissolved fission products factor

κ_{PFP} Precipitated fission products factor

κ_{RD} Radiation damage factor

λ Thermal conductivity

Λ_{eff} Effective prompt neutron generation time

λ_i Delayed neutron precursor decay constant

λ_j Decay heat precursor decay constant

$\mathbb{H}$ Active height of the core

μ Viscosity

ϕ Neutron flux

Π Meyer hardness

Ψ Mean squared roughness

$\Re$ Universal gas constant

ρ Density

$\rho(t)$ Reactivity

σ Stefan-Boltzmann constant

BU Burnup

θ Polar angle

ε Thermal emissivity

ε_{fiss} Energy released per fission

ξ Surface roughness

A Coolant flow area

B_{Xe} Number of xenon atoms born

c Specific heat capacity

$C_i(t)$ Concentration of group i precursors

D Diameter

D_h Hydraulic diameter

f Moody friction factor

F_R	Radial Peaking factor
g	Acceleration of gravity
H	Height
h_j	Relative decay heat power
h_b	Helium gap heat transfer coefficient
h_{Pb}	Cladding-to-coolant heat transfer coefficient
h_{shell}	Height of the spiral tube stack
h_{ss}	Solid-to-solid heat transfer coefficient
h_w	Coolant-to-vessel heat transfer coefficient
K_D	Doppler constant
M	Atomic weight
m	Mass
m_0	Initial mass of fuel
N	Number of fuel assemblies
n	Number of fuel pins
n	Number of moles
$n(t)$	Normalized neutron population
N_A	Avogadro constant
N_{He}	Number of helium atoms
N_{Xe}	Number of xenon atoms released
N_{tube}	Staggered layers per steam generator
Nu	Nusselt number
P	Pitch
P	Pressure
p	Porosity
P_i	Fuel-cladding interface pressure
Pe	Peclet number
q'''	Power density
R	Fuel pellet radius
r	Radial position
R/B	Release-to-birth ratio
$R_{\text{Xe},i}$	Number of xenon atoms released from zone i
Re	Reynolds number
$S(\vec{r})$	Neutron flux spatial distribution
T	Temperature
t	Time
V	Volume
v	Fluid velocity
x	Deviation from stoichiometry
Y_{Xe}	Xenon fission yield
Z	Elevation / Free surface level
z	Axial position

Subscripts and superscripts

PA	Peak assembly
SD	Shut-down state
f	Fuel
g	Gap
c	Cladding
Pb	Coolant
w	Primary vessel
a	Environment
$core$	Core

SG	Steam generator	ctr	Central region
HL	Hotleg	in	Inner region
CL	Coldleg	mid	Middle region
CP	Coldpool	out	Outer region

List of Figures

List of Tables

1 Introduction

Ever since the first commercial Nuclear Power Plant (NPP) started operation in the 1950s, economies of scale have played a key role in addressing nuclear power costs, leading to a strong trend towards the deployment of larger reactors. Utilities have applied economies of scale based on the assumption that the specific capital cost [€/kWe] of a NPP decreases with its power output. Consequently, in developed countries, the size of commercial Light Water Reactor (LWR) units has steadily increased from 60 MWe (*Shippingport*, 1957) to 1600 MWe (*Olkiluoto 3*, to be commissioned in 2022).

1.1 Problem formulation

Following the successful start-up of the first demonstration LWR at Shippingport (Pennsylvania, USA) in 1957, vendors such as Westinghouse Electric and General Electric immediately applied economies of scale to their respective Pressurized Water Reactor (PWR) and Boiling Water Reactor (BWR) designs. By the end of the 1960s, orders were being placed for units over 1000 MWe. Escalating the power output of the plant was prioritized over safety, which instead of being inherent in the reactor design itself, had to be engineered around it. Consequently, multiple core cooling systems had to be implemented to anticipate postulated accidents. Over the next decades, new-built plants were designed according to the same philosophy, meaning that most reactors currently in operation still opt for administrative and engineering controls to ensure their safety.

The overall cost of NPPs is dominated by their capital cost since it represents around 60% of their Levelised Cost Of Electricity (LCOE) (World Nuclear Association, 2017). Therefore, the competitiveness of nuclear power depends on it. Within the 'real' capital cost - also referred to as construction cost - there are two components: the overnight cost and the financing cost. The former takes into account the up-front cost of direct engineering, procurement, and construction services (80%) as well as the owner's cost (20%). Financing costs are incurred when a utility sells equity and/or acquires debt on the financial markets to purchase a power unit. Any form of financing may be described in terms of the Weighted Average Cost of Capital (WACC). In brief, it determines how much interest a utility owes for each dollar it finances, thus a high WACC typically denotes a higher perceived risk associated with a firm's operations. That being said, financing costs are dictated by the time from order to sales of power and the applicable WACC.

On the other hand, plant operating costs (including the cost of fuel, Operation and Maintenance (O&M), decommissioning, and spent fuel management) are relatively low. Therefore, even though the capital-cost component of NPPs is much higher than those of coal and gas-fired plants, the existing nuclear fleet can compete with fossil-fired power plants in the electricity market. Moreover, if penalties on the use of fossil fuels to generate electricity are implemented, the competitiveness of nuclear energy is further enhanced.

Due to the magnitude of the overnight cost of NPPs, in addition to a history of failed projects, embarking on the construction of a large reactor unit is perceived as a high-risk investment. This leads to a higher WACC for nuclear than for any other generation technology. As a result, delays in the time from order to sales of power have a crucial impact on the financing cost, hindering the profitability of new-build nuclear. In 2004, a study by the University of Chicago estimated that the financing cost based on a seven-year construction schedule may constitute

as much as 40% of the overall expenditure for building a large NPP (University of Chicago, 2004). Therefore, irrespective of the overnight cost, the financing cost has proved to be crucial in modern context. Recent Gen III/III+ projects have experienced considerable cost overruns because of construction delays. According to the Nuclear Energy Agency (NEA), delays and consequent cost escalations are to a large extent the result of poor estimates due to the lack of design maturity, especially for a First-Of-A-Kind (FOAK) reactor (NEA, 2020). Furthermore, quality control problems have extensively contributed to overruns in indirect services expenditures - cost of equipment and construction facilities, design services, and commissioning tests - ballooning the capital cost from the high WACC applied over a long construction period.

Throughout the history of the commercial nuclear industry, severe accidents have resulted in additional safety requirements from regulatory authorities. In the immediate aftermath of major nuclear accidents, both existing plants and those under construction have been required to implement design modifications to prevent similar events from occurring in the future, leading to higher overnight costs. In the US, for instance, the Three Mile Island (TMI) accident had a considerable impact on the nuclear industry (Figure 1). In fact, the median costs of those reactors under construction at the time of the accident are 2.8 times higher than pre-TMI costs. This is mainly the result of an increase in construction duration, which rose by a factor of 2.2 with respect to pre-TMI values (Lovering et al., 2016). More recently, since the Fukushima Daiichi accident in 2011, significant developments in active and passive safety features have been implemented in existing NPPs to mitigate the consequences of beyond design basis accidents. To this end, over the last decade, most NPPs are incurring additional expenditures in improvements their design in terms of safety.

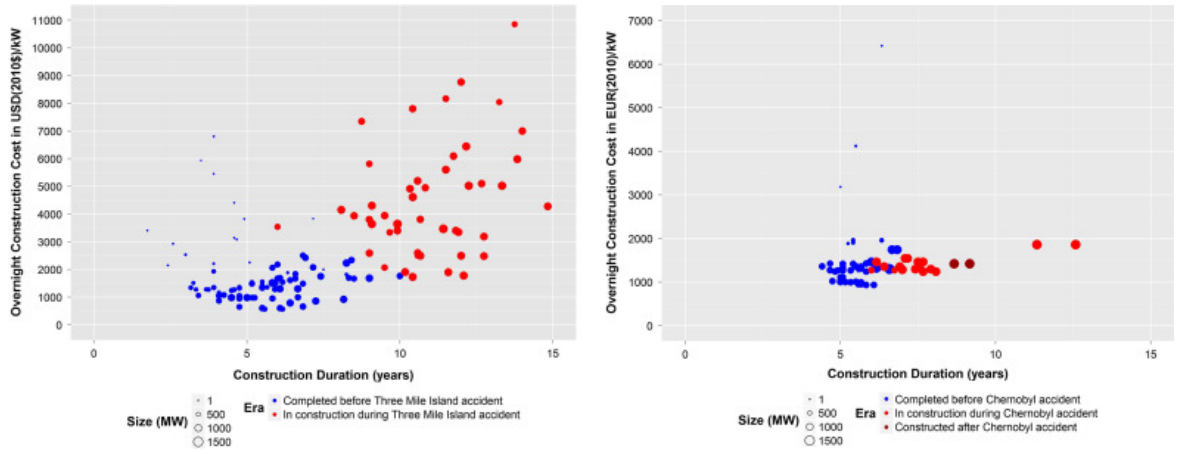

(a) USA (b) France

Figure 1: Overnight cost as a function of construction duration. (Lovering et al., 2016)

Cost escalation has characterized the construction of new NPPs from the first wave of commercial reactors back in the late 1960s to the on-going construction of Gen III+ reactors, compromising the economic viability of the nuclear industry. However, it should also be taken into consideration that most studies in the existing literature focus exclusively on the analysis of cost trends in the USA and France, thus providing an incomplete picture of the worldwide reality. In both countries, historical data reveals a trend towards increasing overnight costs over time, although the cost escalation in France is much milder than in the USA (Figure 1). Contrary

to the cost histories of these countries, a study carried out by Lovering et al. (2016) based on a more complete data set (including the full-cost history of 349 reactors in seven countries) found evidence of declining overnight costs in South Korea. In fact, the South Korean nuclear industry has managed to decline costs by an annual rate of 2% throughout its entire construction experience (Figure 2). These results suggest that cost escalation is not inherent to nuclear power. A detailed analysis of the factors that motivate the large variety in cost trends across different countries is beyond the scope of this thesis. However, it is important to highlight that standardization of reactor designs, multi-siting of reactor units and regulatory stability have proved to be key elements in avoiding the cost escalation path.

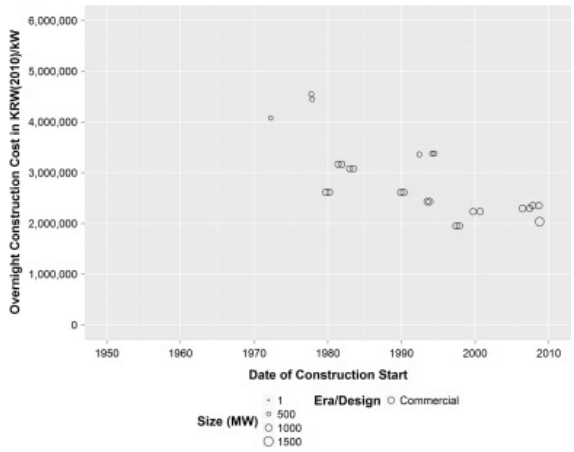

Figure 2: Overnight cost of South Korean nuclear reactors by construction start date. (Lovering et al., 2016)

In the modern context, renewables are prioritized for delivery to the grid for the purpose of reducing greenhouse gases emissions. As a result, other forms of electricity generation are forced to adapt to intermittent renewables whose output depends on occasional wind or solar inputs. This *modus operandi* entails a greater detriment for conventional NPPs than for fossil-fired plants, as a consequence of the former having high fixed operating costs and low variable operating costs, which vary in relation to the output. In conclusion, a single large NPP cannot justify extensive load-following in markets with a high share of variable renewable sources.

1.2 Small modular reactors

The nuclear industry must address the issues faced by the current new-built plants in the western world if it is to remain cost-competitive with other forms of electricity generation, especially in the present context where renewables are favoured by means of subsidies and the cost of natural gas has decreased significantly. Over the last decade, Member States of the International Atomic Energy Agency (IAEA) have made an ongoing effort to research, develop and deploy Small Modular Reactors (SMRs), recognizing their potential as a viable solution to provide reliable, emission-free power generation to the future energy mix. The driving forces in the commercialization of SMRs are mainly two: reducing the total capital cost and thereby the investment risk associated with conventional large NPPs; and providing power to small electricity grids.

On the other side, there are skeptics who claim that SMRs are not cost-competitive with existing nuclear because of the economies of scale principle, which states that the specific capital cost of a reactor decreases with increasing size. Actually, the argument does not seem so far-fetched considering that the move towards developing smaller reactors goes in the opposite direction from the philosophy prevailing during the past five decades. However, it should be noted that economies of scale apply only if the reactors being compared are of a very similar design (Carelli et al., 2010).

The IAEA defines SMRs as advanced nuclear reactors with a power output typically below 300 MWe per module. Their lower electricity output entails smaller transmission infrastructure requirements, thus making SMRs particularly well-suited for deployment in a larger number of locations, especially in remote sites. Furthermore, most designs benefit from a reduced amount of structures, systems, and components. This opens up the possibility of placement below ground level, which would translate into a higher resistance to external threats. But most importantly, a common feature in the design of SMRs is the high degree of modularity, that is, the reliance on serial, factory-based production of stand-alone reactor modules. Compared to Gen II reactor designs, SMRs differ widely in the following areas:

- Modularity
- Scalability
- Safety approach
- Flexibility
- Economics

1.2.1 Modularity

The commercialization of SMRs might resolve the two problems that have been compromising the profitability of new-build reactor projects, that is, long lead times and quality control issues (NEA, 2020). Serial production and inspection of stand-alone units in an automated factory environment significantly simplify the construction phase of the project, leaving site preparation and installation of modules as the only activities to be carried out on the site itself. In addition, factory-based manufacturing of components and subsequent assembly could be done in parallel with site works, hence shortening the deployment schedule (Lokhov et al., 2016). The successful implementation of assembly line production would enable SMRs to profit from the quality assurance that results from standardization, which historically has proved to be a key factor in avoiding costs escalation (Lovering et al., 2016).

1.2.2 Scalability

Modularity and compact size lend themselves to having multiple units on the same site, hence benefiting from serial deployment during the assembly phase. Economies of scale based on the number of units rather than the power output of a single reactor could be achieved by reserving slots for additional units, allowing the plant capacity to be further increased in the future. Even though site permits of some existing NPPs also contemplate this possibility, SMRs elude the high upfront investment associated with large reactor projects, bringing scalability one step forward.

The multi-module configuration offers major advantages regarding refuelling outages. In the first place, small-sized cores allow for a reduction in the number of tasks to execute dur-

ing the process, thereby requiring less human resources. Consequently, in some cases the refuelling and maintenance team could be fully employed by the operator, reducing personnel costs incurred on temporarily subcontracted staff. Secondly, long outage periods could be avoided through sequential unit-by-unit maintenance and refuelling (Lokhov et al., 2016).

1.2.3 Safety approach

An additional reason for the current interest in SMRs is their enhanced nuclear safety. Small-sized cores allow the implementation of unique passive features, to a large extent due to their higher surface-to-volume ratio as compared to large cores. Accordingly, most SMR designs claim to sustain decay heat removal for 24-72h in a completely passive manner by taking advantage of natural phenomena such as gravity, natural convection, and thermal radiation. The use of passive safety systems considerably simplifies the reactor design, reducing the cost associated with the installation and maintenance of active cooling mechanisms that require multiple trains of equipment as well as redundant power supplies. Furthermore, whereas conventional safety systems are highly dependent on active driving devices and operator action, passive safety systems are inherently reliable due to the fact that they rely solely on natural physical laws.

Especially in the post-Fukushima era, the safety approach followed by SMR technologies offers clear advantages in comparison with the so-called mitigation strategy adopted by large NPPs, that is, ensuring safety by increasing the number of protection systems. The implementation of passive features combined with a smaller inventory of radionuclides leads to a substantially smaller source term resulting from a severe accident. This brings up the possibility of reducing the size of the Emergency Planning Zones (EPZs), thus increasing the site flexibility.

1.2.4 Flexibility

The flexibility of SMRs generally refers to the high potential for operation in load-following regimes. In the case of a large NPP, lowering its power output to match electricity demand throughout the day does not entail a significant reduction in plant operating expenses. However, a more cost-effective strategy would consist of maintaining the primary circuit at full power while using the excess heat for cogeneration services such as district heating and cooling, process heat, seawater desalination, and hydrogen production. Cogeneration is envisaged to lead to a drastic reduction in the environmental impact of the nuclear power industry.

Nonetheless, there are several factors that make the integration of large NPPs with co-generational systems considerably more difficult than in the case of SMRs. In the first place, a NPP operating in cogeneration mode must be well-integrated into the existing production facility (e.g., district heating and desalination plant) if thermal losses along the transmission infrastructure are to be minimized. This implies that the plant providing excess heat must be located near the end-user areas, which are often densely populated. Therefore, the size of the EPZs required for large NPPs generally prevents cogeneration applications of GenII reactors. On the other hand, since SMRs are expected to benefit from a reduction of the EPZ, the possibilities of deploying cogeneration plants increase dramatically. Secondly, SMRs are particularly well-suited for cogeneration purposes because their thermal power output is consistent with the thermal load or desalination needs of an urban area. Finally, multi-module configuration offers the possibility to accomplish the load-following strategy at the site level by diverting the

entire thermal power output of some modules to different non-electric applications, while the remaining modules continue generating electricity for the market. That being said, SMR co-generation plants are foreseen to have a crucial role to play in the development of integrated nuclear-renewable energy systems (Lokhov et al., 2016).

To maintain grid stability, the supply and demand of electricity must match at any time. Large reactor units are not suitable for niche electricity markets as they would disrupt the frequency of the grid. This technical requirement prevents large NPPs from being deployed in developing countries with small grids, thus blocking the entry of nuclear power generation into an expanding market. With the advent of SMR technology, many designs are envisioned for small grids and remote regions lacking well-developed transmission infrastructures. In the first case, their inherent scalability could help emerging economies meet the escalating energy demand derived from economic growth and urbanization while reducing dependence on fossil-fired plants. With regard to remote regions, electricity is often produced by means of diesel generators, leading to very high costs for electricity. In these regions, the introduction of SMRs could be an economically feasible strategy to replace diesel.

1.2.5 Economics

Even though there is uncertainty concerning the economics of SMRs, designers claim that their capital cost could be lower than in the case of large LWRs, both in absolute and specific terms (Lokhov et al., 2016). The financing-cost component of recent Gen III+ reactor projects has proved to be the main driver of the cost escalation that called into question the viability of new-build nuclear. However, greater simplicity of the design and economy of series production in an automated factory environment might confer SMR technologies several advantages that should ideally drive down the cost of financing:

- Lower upfront investment required for one unit.
- Reduced time from order to sales of power.
- Lower construction risk resulting from product standardization.

In addition, scalability allows for better management of the investment risk associated with capital-intensive nuclear new-built. It should also be noted that shorter construction times lead to a higher Net Present Value (NPV) of future revenues, thus making projects more viable as investments. All things considered, a multi-module SMR plant may incur smaller financing costs than a single large reactor for a given power output.

The negative impact of economies of scale on the specific overnight cost could be offset by economies of mass production, that is, the manufacturing and assembly of a large number of identical SMRs through optimized supply chains. On this basis, the economic competitiveness of SMRs relies on the profitability of the production facilities, which is determined by the number of units on order. Many vendors claim that their design requires the construction of five to seven units to get the full benefit of the supply chain (Lokhov et al., 2016). However, there is no unanimous consensus on the validity of these estimates as others confidently assert that factory production is not realistic below a hundred units.

Plant operating costs of NPPs are mainly comprised of fixed costs, that is, those incurred whether or not the plant is generating electricity, and therefore independent of its size. As a result, electricity costs per kWh rise substantially when decreasing the power output. Within

operational expenditures, fixed O&M costs include salaries of personnel, site management, preventative and corrective maintenance, etc. Several models have been developed to quantify the O&M costs of SMRs by means of scaling down those incurred in the case of large NPPs (Carelli et al., 2010). The outcome of these models generally consists of a power law of the relative power output

$$\frac{\text{Cost (SMR)}}{\text{Cost (LR)}} \approx \left(\frac{\text{Power (SMR)}}{\text{Power (LR)}} \right)^{\alpha} , \tag{1.1}$$

where LR refers to a large reactor. All models available in the literature use an exponent less than one (typically around 0.5), highlighting a non-linear dependence between the number of units, the power output of the reactor, and the O&M costs. For instance, according to the applicable legislation in several countries, the number of security staff required on-site is independent of the power output of the plant. The current legal framework for nuclear security is tailored to suit the operation of large NPPs, thus the cost of security entails a major drawback for the deployment of SMR projects, especially in the case of projects envisaging a single reactor unit. Nevertheless, many SMRs vendors have proposed innovative solutions for plant operation that might lead to lower O&M costs, such as sharing a single control room among several units or unit-by-unit maintenance and refuelling during outages.

1.2.6 Potential for near-term deployment

The potential mass deployment of SMR technologies is not only founded upon more designs reaching advanced stages of development, but also on their ability to overcome regulatory obstacles that might jeopardize their competitiveness. Therefore, developing a new approach to licensing is indispensable if SMRs are to become a reality in the foreseeable future. In particular, the key issues that should be addressed by the nuclear regulatory bodies are: factory-based manufacturing and ensuing serial deployment of reactor units, personnel requirements for plant operation and security, validation of passive safety systems, and sizing of the EPZ. At the same time, industry and regulatory bodies should work hand-in-hand towards the construction of full-scale prototypes in order to validate the passive safety approach of SMR technologies.

Although there is a large potential for the economics of SMRs, the actual evolution of the market will strongly depend on the successful deployment of prototypes and FOAK plants. Thereafter, the effect of learning will determine the LCOE of future N^{th}-Of-A-Kind (NOAK) reactors. Factory learning rates are expected to considerably reduce costs for NOAK units based on the ability to standardise production. Moreover, higher site-based labour learning rates are foreseen as compared to large NPPs due to a delivery chain that could benefit from the regular production of units (Lewis et al., 2016).

Currently, there are over 50 SMR concepts under development by commercial reactor vendors. According to the SMR booklet published in 2020 by the IAEA (2020), most SMRs can fall into one of these categories:

- Integral LWR (Thermal)
- High Temperature Gas-cooled SMR (Thermal)
- Sodium-cooled SMR (Fast)
- Lead-cooled SMR (Fast)
- Gas-cooled SMR (Fast)
- Molten Salt SMR (Thermal or fast)

1.3 Design of SEALER

SEALER (Swedish Advanced Lead Reactor) is a lead-cooled fast reactor designed by LeadCold Reactors, a spin-off from KTH Royal Institute of Technology (Stockholm) founded by J. Wallenius, P. Szakalos, and J. Ejenstam in 2013. It is intended for commercial power production in the most compact configuration possible, thus benefiting from enhanced passive safety features such as decay heat removal by natural convection. Furthermore, LeadCold Reactors aims to reduce operational expenses and eliminate proliferation concerns through a long-life core design, thereby avoiding on-site refuelling operations during the whole life of the plant. Fast-spectrum reactors are better suited for this purpose owing to their superior breeding performance, that is, the production of fissile fuel from U-238. Additionally, they provide optimal conditions for achieving the transmutation of long-lived, transuranic elements into stable or short-lived isotopes. This reduces the radiotoxicity and volume of the high-level waste inventory at End Of Life (EOL), hence allowing for a more compact arrangement in the final geological repository.

The combined requirement of a long operational lifetime and reduced primary vessel dimensions is best fulfilled by lead coolants. While it is true that gas-cooled reactors using tri-structural isotropic (TRISO) particle fuel are inherently safe and can be engineered in a compact design, their reliance on a thermal neutron spectrum results in a shorter maximum burnup due to their inferior breeding performance. Alternatively, passively cooled reactors driven by natural circulation of liquid sodium may be designed with a breeding ratio larger than unity, thus attaining high levels of fuel burnup. However, due to the fact that sodium exhibits a very small absolute density variation with temperature, these reactors require a higher elevation of the heat exchanger relative to the core as compared to lead-cooled reactors. Apart from the already mentioned excellent potential of liquid lead with respect to decay heat removal by natural convection, which eliminates the need for dedicated emergency core cooling systems, the use of lead as coolant offers several other safety benefits. Some are common among all metal coolants; for example, having a high boiling point. Note that preventing boiling allows the pressure in the primary loop to remain at its nominal value, dramatically reducing the probability of a Loss Of Coolant Accident (LOCA). Other advantages are specific of lead coolants, namely the inherent shielding against gamma radiation emitted from the decay of fission products and the capability to retain iodine, caesium, and polonium in case of fuel cladding failure. As a result, noble gases are the only nuclides having a potentially significant radiological impact in the event of cladding failure. Assuming the confinement fails as well, the release of noble gases to the environment would not require the evacuation of the population residing at the site boundary (Wallenius et al., 2018).

As of today, LeadCold Reactors envisages the deployment of SEALER in two potential markets. To this end, its design has been tailored to meet the specific energy demand of each of these markets, branching out into two different concepts: SEALER-Arctic and SEALER-UK. Target locations for the potential deployment of SEALER-Arctic are off-grid communities and mining sites in the Canadian and Swedish Arctic, where electricity and heat are often produced by means of diesel generators. The lack of permanent transport infrastructures prevents access to a steady supply of diesel fuel, meaning that on-site transportation is not only expensive but completely dependent on weather conditions. On top of that, the cost of storing diesel fuel further increases the price of electricity and heat. In this scenario, SEALER-Arctic holds the potential to replace diesel generators at a competitive cost. On the other hand, SEALER-UK is intended to provide base-load power for the United Kingdom's national grid.

The dynamic behaviour of a nuclear reactor system is intrinsically difficult to model due to a large number of parameters involved and their intricate dependencies. Human reasoning and simple theoretical models are simply not capable of untangling the outcome of the system in response to a perturbation. For this reason, system codes play a critical role in the design and safety analysis of nuclear reactors. Several system codes have been developed for fast reactor transient analysis. However, complexity and relatively restricted access to the source code for modifying built-in models and correlations make their use for safety-informed reactor design rather cumbersome. In this context, BELLA (Bortot's Elegant Liquid LFR Analysis tool) is conceived as a simple, easily modifiable, yet adequate computer code for dynamic transient simulation of fast reactors.

BELLA was employed in all transient simulations performed within the framework of this thesis based on the design parameters of SEALER-Arctic.

Table 1: Major technical parameters of SEALER. (Wallenius et al., 2018; Wallenius et al., 2019)

Parameter	**SEALER-Arctic**	**SEALER-UK**
Power output (MW/MWe)	8/3	140/55
Core inlet temperature (ºC)	390	420
Core outlet temperature (ºC)	432	550
Fuel type	UO_2	UN
Fuel enrichment (%)	19.75	11.8
Fuel burnup (GWd/ton)	33	60
Core lifetime (yr*)	30	25
Fuel assemblies	19	85
Fuel rods per assembly	91	217
Primary vessel outer diameter (m)	2.748	4.180
Vessel total height (m)	6.0	6.0
Power density (W/cm^3)	30	112

(*) Assuming an availability of 90 %.

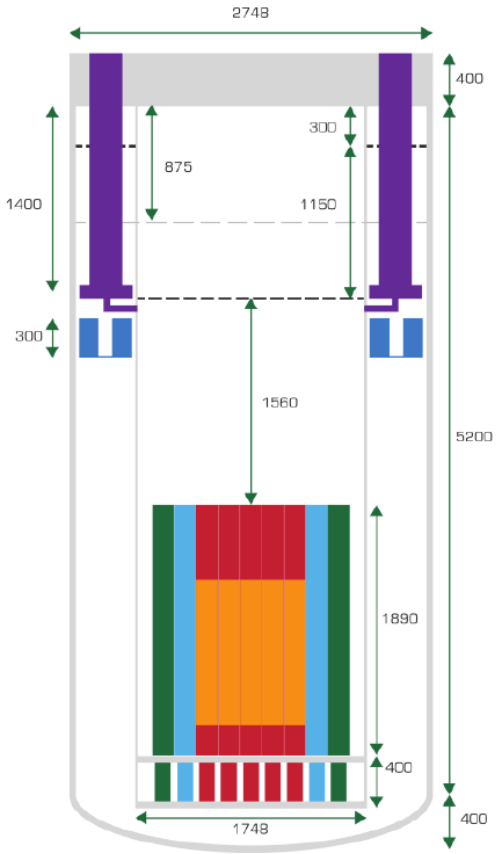

Figure 3: SEALER-Arctic primary system elevations. (Wallenius et al., 2018)

2 BELLA reference model

BELLA is a system code intended for use in the safety-informed, conceptual design of lead-cooled fast reactors. Simulations of their dynamic behaviour under design basis and beyond design basis accidents are based on a lumped-parameters approach for the time-dependent coupling between thermal-hydraulics and neutron kinetics. BELLA models the primary system as a collection of single points comprised of the reactor core, steam generator, hot leg, cold leg, and cold pool, featuring average and boundary temperatures. The differential equations describing the kinetic behaviour of the reactor are derived using the point kinetics approximation. With regard to thermal-hydraulics, balance equations of energy, momentum, and mass are applied to all primary components, resulting in another set of coupled differential equations. Finally, a rough estimation of the heat source introduced by the radioactive decay of ^{235}U fission products is provided.

Current capabilities of BELLA include simulation of limiting transients identified as Unprotected Transient Over-Power (UTOP), Loss Of Flow (ULOF), and Loss Of Heat Sink (ULOHS), in addition to reactor SCRAM.

2.1 Neutron kinetics

In short, the point kinetics approximation consists of splitting the neutron flux $\phi(\vec{r}, t)$ into two factors

$$\phi(\vec{r}, t) = S(\vec{r})\, n(t)\ , \tag{2.1}$$

where $S(\vec{r})$ denotes a shape function depending only on space, whereas $n(t)$ is a time-dependent amplitude function. The choice of these functions is arbitrary provided that their product yields the neutron flux, thus $S(\vec{r})$ and $n(t)$ can be defined in a way such that the latter represents the dimensionless neutron population in the reactor core. On the other hand, the spatial distribution of the neutron flux, however defined, remains unchanged during transient calculations as a consequence of assuming a space-time separated function to describe $\phi(\vec{r}, t)$. This implies that $S(\vec{r})$ can be determined from the reactor initial state (before perturbations are applied). For instance, the one-group diffusion equation can be solved analytically for a homogeneous, non-reflected, cylindrical reactor. In that particular case, the spatial distribution of the neutron flux is given by

$$S(r, z) = J_0\left(\frac{2.405r}{\widetilde{R}}\right)\cos\left(\frac{\pi z}{\widetilde{\mathbb{H}}}\right)\ , \tag{2.2}$$

where $\widetilde{R}$ and $\widetilde{\mathbb{H}}$ represent the extrapolated radius and active height of the core respectively, and J_0 is the Bessel function of the first kind of order zero. Due to the fact that fast neutrons have a larger mean free path than thermal neutrons, the point kinetics approximation is better valid for fast reactors, providing reasonably high accuracy.

The direct-fission component of the reactor power level $\dot{Q}(t)$ is directly linked to the neutron flux, hence the time-dependent neutron population. To simplify the upcoming mathematical expressions, the latter variable is normalized to its steady-state value, meaning that the initial condition $n(0) = 1$ is fulfilled. Then, the reactor power is given by

$$\dot{Q}(t) = \dot{Q}(0)\, n(t)\ , \tag{2.3}$$

where $\dot{Q}(0)$ refers to the steady-state reactor power and contains the spatial distribution of the neutron flux. In the one-group point kinetics approximation using 8 delayed neutron precursor groups, the neutron population evolution over time can be described as

$$\frac{dn(t)}{dt} = \frac{\rho(t) - \beta_{\text{eff}}}{\Lambda_{\text{eff}}} n(t) + \sum_{i=1}^{8} \lambda_i C_i(t) \;\; ; \;\; \beta_{\text{eff}} = \sum_{i=1}^{8} \beta_i \; , \tag{2.4}$$

where $\rho(t)$ represents the time-dependent reactivity, λ_i is the decay constant of the *i*-th delayed neutron precursor group, β_{eff} is the total effective delayed neutron fraction calculated as the sum of individual effective fractions β_i, and Λ_{eff} is the so-called effective prompt neutron generation time, that is, the mean time that it takes for a prompt fission neutron to produce a new prompt fission neutron. It is worth mentioning that the neutronic parameters β_i and Λ_{eff} only drop their time dependence within the point kinetics approximation. The concentration of precursors in the *i*-th group $C_i(t)$ varies over time according to

$$\frac{dC_i(t)}{dt} = \frac{\beta_i}{\Lambda_{\text{eff}}} n(t) - \lambda_i C_i(t) \; . \tag{2.5}$$

From the above equation, the normalized, equilibrium concentration of the *i*-th precursor group is obtained by equating the time derivative to zero and plugging in the initial condition for the neutron population, yielding

$$C_i(0) = \frac{\beta_i}{\Lambda_{\text{eff}} \lambda_i} \; . \tag{2.6}$$

The coupling between thermal-hydraulics and neutron kinetics entails continuous reactivity feedback due to coolant and fuel temperature variations. As far as fast reactors are concerned, the main contributions to reactivity feedback arise from the Doppler broadening in the fuel, axial expansion of the fuel, changes in coolant density, and radial expansion of the fuel assembly foot diagrid. The differential change in reactivity $\delta\rho(t)$ given a small change of temperature may be approximated by

$$\delta\rho(t) = K_D \ln\left(\frac{\bar{T}_f(t)}{\bar{T}_f(0)}\right) + \alpha_{axial}\delta\bar{T}_f(t) + \alpha_{Pb}\delta\bar{T}_{Pb}(t) + \alpha_{radial}\delta T^{in}_{Pb}(t) \; , \tag{2.7}$$

where K_D is the Doppler constant, $\bar{T}_f$ and $\bar{T}_{Pb}$ are the average fuel and core coolant temperature respectively, and T^{in}_{Pb} is the coolant temperature at the core inlet plenum. The parameters α_{axial}, α_{Pb} and α_{radial} denote fuel axial expansion, coolant temperature, and diagrid radial expansion reactivity feedback coefficients respectively. It should be noticed that all coefficients are assumed to be independent of temperature.

2.2 Thermal-hydraulics

2.2.1 Energy balance equations

The heat transfer between core components can be modelled by writing a set of energy balance differential equations for fuel (f), cladding (c), and coolant (Pb). The radial mesh structure adopted in BELLA to calculate temperatures in the core is shown in Figure 4. Three radial nodes are used in the fuel pellet, three more in the cladding, and one in the coolant. Note that the first and last nodes of any core component are always half size. The reference BELLA code

does not take into account the thermal expansion of the fuel and cladding due to temperature variations, meaning that radii of all nodes described in the mesh will remain unchanged throughout transient calculations. Regarding the axial mesh structure, the whole active height of the core, that is, the height of the fuel pellet column, is represented by a single node of length $\mathbb{H}$. Thus, the temperature distribution along the axial direction is not considered.

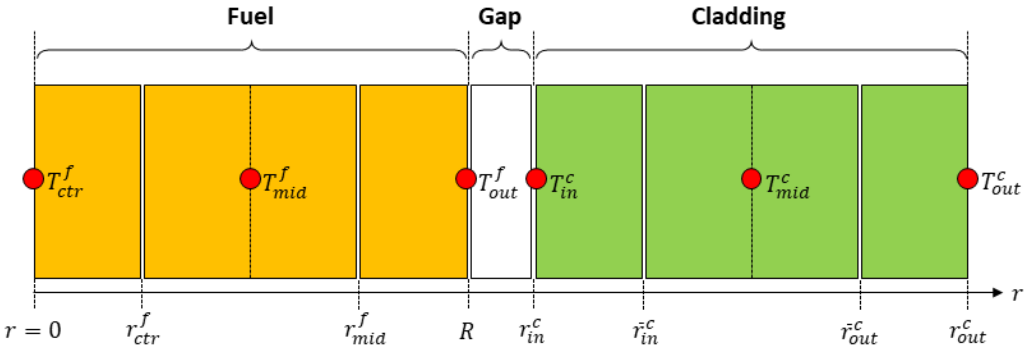

Figure 4: Radial nodalization for fuel and cladding.

The most general heat transfer equation in conduction-dominated energy balances can be written in cylindrical coordinates as

$$\rho c \frac{\partial T}{\partial t} = \frac{1}{r}\frac{\partial}{\partial r}\left(\lambda r \frac{\partial T}{\partial r}\right) + q''' \,, \tag{2.8}$$

where ρ is the density, c is the specific heat capacity, λ is the thermal conductivity, and q''' is the power density. Based on the assumption that power is generated exclusively within the fuel pellet, the last term in the above equation vanishes in the case of cladding. Applying finite differences in the radial direction to eq. (2.8) yields

$$\begin{aligned} m_i c \frac{\partial T_i}{\partial t} &= \frac{\pi\left[(r_i+\Delta r)^2 - r_i^2\right]\mathbb{H}n}{(r_i+\Delta r/2)\,\Delta r}\left[\lambda_{i,i+1} r_{i+1}\frac{T_{i+1}-T_i}{\Delta r} - \lambda_{i-1,i} r_i \frac{T_i - T_{i-1}}{\Delta r}\right] + \dot{Q}_i \\ &\underset{\Delta r\to 0}{\simeq} 2\pi\mathbb{H}n\left[\lambda_{i,i+1} r_{i+1}\frac{T_{i+1}-T_i}{\Delta r} - \lambda_{i-1,i} r_i \frac{T_i - T_{i-1}}{\Delta r}\right] + \dot{Q}_i \,, \end{aligned} \tag{2.9}$$

where m_i and $\dot{Q}_i$ denote respectively the mass and the power generation associated with the i-th radial node, n is the number of fuel pins in the core, and Δr is the radial difference mesh.

The first term on the right-hand side of eq. (2.8) relates to the heat flux entering/exiting a volume of material. In the case of solid core components such as fuel and cladding, conduction is the dominant heat transfer mechanism and the heat flux is adequately described by Fourier's law. Nevertheless, other heat transfer processes can be included by arbitrarily redefining the source term q''' to represent a radiation term or a convective heat flux into a fluid. For instance, the heat flux from the fuel outer surface to the cladding inner wall contains both a radiation term ($\dot{Q}_{rad}$) and a helium bond conductance term ($\dot{Q}_b$). The former is described in terms of the Stefan-Boltzmann formula multiplied by an emissivity correction factor

$$\dot{Q}_{rad} = 2\pi R\mathbb{H}n\,\frac{\sigma}{\dfrac{1}{\varepsilon_f}+\dfrac{1}{\varepsilon_c}-1}\left[(T^f_{out})^4 - (T^c_{in})^4\right] \,, \tag{2.10}$$

where σ is the Stefan-Boltzmann constant, and ε_f and ε_c denote the fuel and cladding emissivity respectively. On the other hand, the conductance term contains an effective heat transfer coefficient h_b having units of W/K, which takes into account the presence of helium in the gap separating the fuel pellet and the cladding. Its mathematical expression is obtained by integrating the differential form of Fourier's law over the volume of the gap

$$\dot{Q}_b(r) = 2\pi r \mathbb{H} n \lambda_{\mathrm{He}} \frac{\partial T}{\partial r} \approx h_b \left(T^f_{out} - T^c_{in} \right) \; ; \; r \in [R, r^c_{in}] \; \rightarrow \; h_b = \frac{2\pi \mathbb{H} n \lambda_{\mathrm{He}}}{\ln\left(\frac{r^c_{in}}{R} \right)} \, , \tag{2.11}$$

where r^c_{in} is the cladding inner radius and R is the fuel pellet radius. Lastly, the convective heat transfer coefficient h_{Pb} between the outer cladding surface and the coolant flowing in the core includes dimensional factors and is calculated as

$$h_{Pb} = 2\pi r^c_{out} \mathbb{H} n \lambda^{core}_{Pb} \frac{Nu^{core}_{Pb}}{D^{core}_h} \, , \tag{2.12}$$

in which r^c_{out} is the cladding outer radius, D^{core}_h is the hydraulic diameter of the core, and Nu^{core}_{Pb} is the Nusselt number calculated according to Mikityuk (2009).

With this information, the evolution of the fuel, cladding and core coolant temperatures can be evaluated by solving the following set of first order differential equations:

$$\begin{aligned}
m^f_{ctr} c_f \frac{dT^f_{ctr}}{dt} &= \dot{Q}_{ctr} - \frac{2\pi r^f_{ctr} \mathbb{H} n \lambda^f_{ctr,mid}}{R/2} \left(T^f_{ctr} - T^f_{mid} \right) \\
m^f_{mid} c_f \frac{dT^f_{mid}}{dt} &= \dot{Q}_{mid} - \frac{2\pi r^f_{mid} \mathbb{H} n \lambda^f_{mid,out}}{R/2} \left(T^f_{mid} - T^f_{out} \right) + \frac{2\pi r^f_{ctr} \mathbb{H} n \lambda^f_{ctr,mid}}{R/2} \left(T^f_{ctr} - T^f_{mid} \right) \\
m^f_{out} c_f \frac{dT^f_{out}}{dt} &= \dot{Q}_{out} + \frac{2\pi r^f_{mid} \mathbb{H} n \lambda^f_{mid,out}}{R/2} \left(T^f_{mid} - T^f_{out} \right) - h_b \left(T^f_{out} - T^c_{in} \right) - \dot{Q}_{rad} \\
m^c_{in} c_c \frac{dT^c_{in}}{dt} &= -\frac{2\pi \bar{r}^c_{in} \mathbb{H} n \lambda^c_{mid}}{\delta_c/2} \left(T^c_{in} - T^c_{mid} \right) + h_b \left(T^f_{out} - T^c_{in} \right) + \dot{Q}_{rad} \\
m^c_{mid} c_c \frac{dT^c_{mid}}{dt} &= -\frac{2\pi \bar{r}^c_{out} \mathbb{H} n \lambda^c_{mid}}{\delta_c/2} \left(T^c_{mid} - T^c_{out} \right) + \frac{2\pi \bar{r}^c_{in} \mathbb{H} n \lambda^c_{mid}}{\delta_c/2} \left(T^c_{in} - T^c_{mid} \right) \\
m^c_{out} c_c \frac{dT^c_{out}}{dt} &= \frac{2\pi \bar{r}^c_{out} \mathbb{H} n \lambda^c_{mid}}{\delta_c/2} \left(T^c_{mid} - T^c_{out} \right) - h_{Pb} \left(T^c_{out} - \bar{T}^{core}_{Pb} \right) \\
m^{core}_{Pb} c_{Pb} \frac{dT^{core}_{out}}{dt} &= h_{Pb} \left(T^c_{out} - \bar{T}^{core}_{Pb} \right) - \dot{m}^{core}_{Pb} c_{Pb} \Delta T^{core}_{Pb} \, ,
\end{aligned} \tag{2.13}$$

where r^f_i refers to the outer radius of the *i*-th fuel zone, δ_c is the thickness of the cladding, $\bar{r}^c_{in}$ is the outer radius of the inner cladding zone, $\bar{r}^c_{out}$ is the inner radius of the outer cladding zone, $\bar{T}^{core}_{Pb} = \left(T^{core}_{out} + T^{core}_{in} \right)/2$ is the average core coolant temperature, and $\Delta T^{core}_{Pb} = T^{core}_{out} - T^{core}_{in}$ is the coolant temperature rise between outlet and inlet of the core. The heat transfer equations shown above are coupled to the rest of the primary system by means of the mass flow rate $\dot{m}^{core}_{Pb}$ of coolant circulating through the reactor core.

The thermal conductivity at the interface of two adjacent fuel nodes is evaluated at their average temperature. As for the cladding, its node-to-node changes in temperature are of the

order of 1 ºC, thus its thermal conductivity is calculated at the cladding mid-point and assumed equal for all nodes. Specific heat capacities of core components are updated at the beginning of every simulation time step based on the previous step solution, then treated as parameters when solving the energy balance equations. The reason behind this simplification is that specific heat capacity does not significantly vary over the temperature range incurred in a single time step calculation. By contrast, the temperature dependence of thermal conductivity is explicitly taken into account in the formulation of the heat transfer equations implemented in BELLA. That said, fuel and cladding specific heat capacities are evaluated at the average fuel temperature and cladding mid-point temperature respectively. The former is calculated as the mass-weighted average over central, middle, and outer fuel zones, and is also used in eq. (2.7) to estimate the reactivity feedback

$$\bar{T}_{fuel} = \left(\frac{r_{ctr}^2}{R^2}\right) T_{ctr}^f + \left(\frac{r_{mid}^2 - r_{ctr}^2}{R^2}\right) T_{mid}^f + \left(\frac{R^2 - r_{mid}^2}{R^2}\right) T_{out}^f \,. \tag{2.14}$$

The steady-state solution of fuel (central, middle, and outer nodes) and cladding (inner and middle nodes) temperatures are computed numerically from the transient equations equating all time derivatives to zero. As for the core coolant mass flow rate and outer cladding temperature, both variables are previously initialized by requiring that the total power generated in the fuel be transferred to the coolant circulating in the core. Note that this condition can be derived by combining the steady-state energy balance equations written for fuel and cladding. In BELLA, the user is required to manually input the nominal value of three primary side parameters: coolant temperature at the core inlet, coolant temperature rise across the core, and thermal power output. Then, performing simple steady-state arithmetic based on the input parameters, in addition to geometrical parameters, leads to

$$\begin{cases} \dot{Q} = \dot{m}_{Pb}^{core} c_{Pb} \Delta T_{Pb}^{core} \\ \dot{Q} = h_{Pb} \left(T_{out}^c - \bar{T}_{Pb}^{core}\right) \end{cases} \rightarrow \begin{cases} T_{out}^c = \bar{T}_{Pb}^{core} + \dfrac{\dot{Q} D_h^{core}}{2\pi r_{out}^c \mathbb{H} n \lambda_{Pb}^{core} Nu_{Pb}^{core}} \\ \dot{m}_{Pb}^{core} = \dfrac{\dot{Q}}{c_{Pb} \Delta T_{Pb}^{core}} \end{cases} . \tag{2.15}$$

The specific heat capacity, thermal conductivity, and Nusselt number in the above equation are evaluated at the average core coolant temperature and velocity, the latter being determined from the mass flow rate and the flow area as

$$\bar{v}_{Pb}^{core} = \frac{\dot{m}_{Pb}^{core}}{A_{Pb}^{core} \bar{\rho}_{Pb}^{core}} \,. \tag{2.16}$$

Heat transfer in the rest of the primary system components -steam generator (SG), hot leg (HL), cold leg (CL), and cold pool (CP)- is approximated by the following set of energy balance equations:

$$\begin{aligned} m_{Pb}^{HL} \frac{d\bar{T}_{Pb}^{HL}}{dt} &= \dot{m}_{Pb}^{core} \left(T_{out}^{core} - \bar{T}_{Pb}^{HL}\right) \\ m_{Pb}^{CL} c_{Pb} \frac{d\bar{T}_{Pb}^{CL}}{dt} &= \dot{m}_{Pb}^{SG} c_{Pb} \left(T_{out}^{SG} - \bar{T}_{Pb}^{CL}\right) - h_w \left(\bar{T}_{Pb}^{CL} - \bar{T}_w\right) \\ m_w c_w \frac{d\bar{T}_w}{dt} &= h_w \left(\bar{T}_{Pb}^{CL} - \bar{T}_w\right) - \frac{A_w \sigma}{\dfrac{1}{\varepsilon_w} + \dfrac{1}{\varepsilon_a} - 1} \left(\bar{T}_w^4 - T_a^4\right) \\ m_{Pb}^{CP} \frac{dT_{Pb}^{CP}}{dt} &= \dot{m}_{Pb}^{core} \left(\bar{T}_{Pb}^{CL} - T_{Pb}^{CP}\right) \,, \end{aligned} \tag{2.17}$$

where the subscript w refers to the primary vessel wall, being ε_w its emissivity, ε_a denotes the ambient emissivity, and the specific heat capacity in the second equation c_{Pb} is evaluated at the cold leg temperature resulting from the previous time step calculation. Note that the environment is assumed as an infinite heat sink with constant temperature T_a. For simplicity, the mass flow in the cold leg is assumed to equal that in the steam generator, whereas in the case of hot leg and cold pool, these are set equal to the mass flow in the core. These approximations are valid as long as the frictional pressure drops across the hot leg, cold leg, and pool volumes are negligible in comparison to that in the core and steam generator. Further calculations based on the Darcy-Weisbach equation (see subsection 2.2.4) and the design parameters of SEALER show that these conditions are indeed fulfilled. Note that coolant mass in the cold leg and hot leg can be expressed in terms of their corresponding free surface levels Z^{CL}, Z^{HL} as

$$\begin{aligned} m_{Pb}^{HL} &= A_{Pb}^{HL}\rho_{Pb}^{HL}Z^{HL} \\ m_{Pb}^{CL} &= A_{Pb}^{CL}\rho_{Pb}^{CL}Z^{CL} \,, \end{aligned} \tag{2.18}$$

where A_{Pb} is the cross-sectional area of the flow. The reference BELLA code accounts for the fact that a fraction of the heat dissipated into the coolant is eventually transferred to the primary vessel as it flows through the cold leg. The convective heat transfer coefficient h_w between the the coolant circulating in the cold leg and the inner wall of the vessel (including dimensional factors) is calculated using the correlation suggested by Seban and Shimazaki (1951) for the Nusselt number

$$h_w = 2\pi r_{in}^w Z^{CL}\left[5 + 0.025\left(Pe_{Pb}^{CL}\right)^{0.8}\right]\frac{\lambda_{Pb}^{CL}}{D_h^{CL}} \,, \tag{2.19}$$

where the cold leg free surface level is measured relative to the inlet of the cold pool, r_{in}^w is the inner radius of the vessel, and Pe_{Pb}^{CL} refers to the Peclet number. The thermal conductivity λ_{Pb}^{CL} is evaluated at the cold leg temperature. At the same time, the primary vessel radiates heat from its outer surface A_w to the environment. Thus, the heat transfer equation describing the evolution of the vessel temperature also includes a radiation term. The net heat exchange through radiation is calculated from the Stefan-Boltzmann law with an emissivity correction factor, which depends on the emissivities of the material that constitutes the vessel and the ambient.

None of the energy balance equations presented above explicitly includes a time derivative of the steam generator temperature, which in principle would enable to determine its evolution throughout the transient. The current version of BELLA cannot perform a detailed thermal-hydraulic simulation of the steam/water secondary circuit. Nevertheless, it provides two different approaches to modelling heat transfer from the primary to the secondary side of the steam generators. These options consist of imposing any user-defined function for either power removal $\dot{Q}_{SG}$ or temperature difference between the inlet and the outlet ΔT_{Pb}^{SG}

$$\begin{aligned} T_{out}^{SG} &= T_{in}^{SG} - \frac{\dot{Q}_{SG}}{c_{Pb}\dot{m}_{Pb}^{SG}} \\ T_{out}^{SG} &= T_{in}^{SG} - \Delta T_{Pb}^{SG} \,. \end{aligned} \tag{2.20}$$

Both the rate of heat removal to the secondary system and the temperature drop in the steam generator primary side are user-defined input parameters, hence remain constant during the transient calculation. Finally, the coolant temperature at the inlet of the steam generator T_{in}^{SG} is assumed to equal the average temperature in the hot leg

$$T_{in}^{SG} = \bar{T}_{Pb}^{HL} \,. \tag{2.21}$$

The steady-state temperatures are obtained by setting to zero all the time derivatives that appear in the energy balance equations, then solving the resulting system of linear equations.

2.2.2 Momentum balance equations

The time evolution of mass flow rates across the core and steam generators are calculated by integrating the momentum balance equation for a one-dimensional, single-phase, incompressible flow

$$\frac{d(\rho v)}{dt} = -\frac{\partial\left(\rho v^2\right)}{\partial z} - \frac{\partial P}{\partial z} - \rho g \cos\theta - F_{fr} \ , \tag{2.22}$$

over the height of the component in question (hereafter referred to as H). Then, re-writing the resulting expression in terms of the mass flow rate $\dot{m}$ instead of the fluid velocity v yields

$$\begin{aligned} \frac{d\dot{m}}{dt} &= -\frac{A}{H}\left[\frac{\dot{m}^2}{A^2}\left(\frac{1}{\rho_{out}} - \frac{1}{\rho_{in}}\right) + \Delta P_{HS} + \rho g H \cos\theta + \Delta P_{fr}\right] \\ &\approx -\frac{A}{H}\left[\Delta P_{HS} + \rho g H \cos\theta + \Delta P_{fr}\right] \ , \end{aligned} \tag{2.23}$$

where A is the cross-sectional area of the flow. The term containing (inverse) density differences between the outlet and inlet of the component was neglected based on the Boussinesq approximation. Despite the fact that the primary circulation of SEALER is not driven by natural convection during nominal operation, as justified in detail below, this approximation is still accurate over the range of mass flows involved in the simulations. In fact, under steady-state conditions, the term in question is four orders of magnitude smaller than the gravity-head term, thus would only entail a higher-order correction to the results of the transient calculation.

That being said, the first term on the right-hand side of eq. (2.23) stands for the hydrostatic pressure gradient between the outlet and the inlet of the component. The second term is the gravity-head pressure, where g is the gravitational constant and θ refers to the angle of coolant flow motion relative to the vertical axis. As far as the hot leg is concerned, the coolant flows upwards from the core outlet to the steam generator inlet, thus $\cos\theta = 1$ and the gravity-head term contributes negatively to the mass flow variation over time. On the contrary, the coolant in the cold leg flows downwards from the outlet of the steam generator to the inlet of the cold pool, meaning that $\cos\theta = -1$. Therefore, in this case, the pressure head induced by gravity favours an increase in the mass flow rate. Finally, the last term takes into account the viscous forces F_{fr} in the vertical direction, which result in a pressure drop ΔP_{fr} across the component. The minus sign highlights the fact that it is always a loss term.

The hydrostatic pressure difference between the outlet and the inlet of the core and steam generator can be written as a function of free surface levels and coolant densities.

$$\begin{aligned} \Delta P_{HS}^{core} &= P_{out}^{core} - P_{in}^{core} = g\left(\bar{\rho}_{Pb}^{HL} Z^{HL} - \bar{\rho}_{Pb}^{CL} Z^{CL}\right) \\ \Delta P_{HS}^{SG} &= P_{out}^{SG} - P_{in}^{SG} = g\bar{\rho}_{Pb}^{CL}\left(Z^{CL} - Z^{SG} - H^{core}\right) - g\bar{\rho}_{Pb}^{HL}\left(Z^{HL} - Z^{SG} - H^{SG}\right) \ , \end{aligned} \tag{2.24}$$

where Z^{SG} is the elevation of the steam generator relative to the outlet of the core, H^{SG} refers to the height of the steam generator, and H^{core} is the height of the core (from coolant inlet to coolant outlet). It is important to note the difference between the latter parameter and the active height of the core (H) used in subsection 2.2.1 while dealing with heat transfer between

core components. Under nominal conditions, the hydrostatic pressure gradient across the core is negative since the coolant temperature at the outlet is higher, meaning that its density is lower, and the cold leg free surface level is higher compared to that of the hot leg. Therefore, ΔP_{HS}^{core} is the only term driving the flow towards the outlet of the core. Applying the same reasoning to the steam generator results in a positive hydrostatic pressure gradient. Consequently, ΔP_{HS}^{SG} turns out to be a loss term, same as the frictional pressure drop, and the only driving force pushing the coolant downwards to the inlet of the cold leg is gravity.

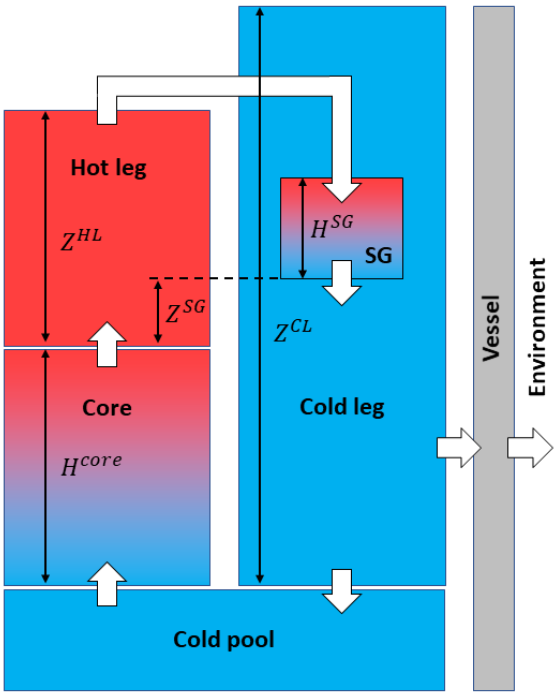

Figure 5: Primary system nodalization in BELLA.

Nevertheless, to compensate for the head losses incurred under nominal operation, the design of SEALER foresees the installation of several variable speed reactor coolant pumps (Wallenius et al., 2018), thus relying on forced circulation. The suction side of each pump is connected to the hot leg. Then, the coolant is discharged into the plenum above the steam generator. The combined pump-head pressure increase from all the pumps in the primary system ΔP_{pump} is taken into account in the momentum balance equation written for the steam generator.

With this information, the change in mass flow rates across the core and steam generator is calculated as

$$\begin{aligned} \frac{d\dot{m}_{Pb}^{core}}{dt} &= -\frac{A_{Pb}^{core}}{H^{core}}\left[\Delta P_{HS}^{core} + g\bar{\rho}_{Pb}^{core}H^{core} + \Delta P_{fr}^{core}\right] \\ \frac{d\dot{m}_{Pb}^{SG}}{dt} &= -\frac{A_{Pb}^{SG}}{H^{SG}}\left[\Delta P_{HS}^{SG} - g\bar{\rho}_{Pb}^{SG}H^{SG} + \Delta P_{fr}^{SG} - \Delta P_{pump}\right] . \end{aligned} \tag{2.25}$$

By setting the time-derivative terms to zero in the above equations, the following steady-state conditions are obtained:

$$0 = g\left(\bar{\rho}_{Pb}^{HL} Z^{HL} - \bar{\rho}_{Pb}^{CL} Z^{CL}\right) + g\bar{\rho}_{Pb}^{core} H^{core} + \Delta P_{fr}^{core} \tag{2.26a}$$

$$0 = g\bar{\rho}_{Pb}^{CL}\left(Z^{CL} - Z^{SG} - H^{core}\right) - g\bar{\rho}_{Pb}^{HL}\left(Z^{HL} - Z^{SG} - H^{SG}\right) - g\bar{\rho}_{Pb}^{SG} H_{SG} + \Delta P_{fr}^{SG} - \Delta P_{pump}\,. \tag{2.26b}$$

All coolant densities are evaluated at the steady-state temperature of their respective component. Frictional pressure drops across the core and steam generator at $t = 0$ are calculated as described in subsection 2.2.4. The above system of equations contains three unknowns: the steady-state hot leg and cold leg free surface levels, and the pump-head pressure. Adding the two equations eliminates the variables Z^{HL} and Z^{CL}, thus

$$\begin{aligned}\Delta P_{pump} = {} & g\bar{\rho}_{Pb}^{core} H^{core} + \Delta P_{fr}^{core} - g\bar{\rho}_{Pb}^{CL}\left(Z^{SG} + H^{core}\right) \\ & + g\bar{\rho}_{Pb}^{HL}\left(Z^{SG} + H^{SG}\right) - g\bar{\rho}_{Pb}^{SG} H^{SG} + \Delta P_{fr}^{SG}\,.\end{aligned} \tag{2.27}$$

Note that the result only depends on the design characteristics of SEALER and steady-state coolant densities. The pump-head pressure calculated as in eq. (2.27) can be interpreted as the minimum pressure required to offset all the head losses in the core and steam generator combined. Introducing the expression derived for ΔP_{pump} into the momentum balance equation leads to a null pressure change across the entire primary loop under steady-state operation, that is, constant mass flow rates. By proceeding this way, conditions stated in (2.26) are now reduced to a single equation with two unknowns, which means that the problem is ill-defined.

While the reactor is in cold Shut-Down (SD), all system temperatures equal to 663 K. In this state, pumps do not operate at their nominal capacity and the coolant free surface levels are equalised. Nevertheless, during normal operation conditions, forced circulation of the coolant is required in order to achieve the desired temperature rise over the core, hence the need for including pumps in the design of the primary system. As a consequence of the driving force introduced by the pumps, the free surface level in the hot leg drops relative to its shutdown value, whereas the opposite occurs as regards the cold leg. This reasoning provides an alternative interpretation of the term ΔP_{pump} based on the difference in hot and cold leg free surface levels, which can be written in mathematical form as

$$\Delta P_{pump} = g\bar{\rho}_{Pb}^{CL}\left[\left(Z^{CL} - H^{core}\right) - Z^{HL}\right]\,. \tag{2.28}$$

One would be tempted to conclude that by setting the above equation as an additional constraint to the ill-defined problem stated in (2.26), the unknowns Z^{CL} and Z^{HL} can be uniquely determined. However, as it turns out, the expression above is a linear combination of the equations that constitute such a problem, meaning that yet another constraint must be imposed if the solution is to be unique.

In BELLA, the extra degree of freedom is removed by applying the mass conservation principle to the coolant in the hot leg and cold leg, that is, the total mass of coolant in these two components combined, must be the same during nominal operation and cold shut-down. Therefore,

$$A_{Pb}^{HL}\bar{\rho}_{Pb}^{HL} Z^{HL} + A_{Pb}^{CL}\bar{\rho}_{Pb}^{CL} Z^{CL} = A_{Pb}^{HL}\rho_{Pb}^{SD}\left(Z^{SD} - H^{core}\right) + A_{Pb}^{CL}\rho_{Pb}^{SD} Z^{SD}\,, \tag{2.29}$$

where Z^{SD} is the free surface elevation relative to the cold pool during shut-down and ρ_{Pb}^{SD} is the coolant density evaluated at 663 K. Isolating Z^{HL} in both eqs. (2.29) and (2.26a), and then equaling the obtained expressions, gives the cold leg free surface level

$$Z^{CL} = \frac{1}{\bar{\rho}_{Pb}^{CL}\left(1 + A_{Pb}^{CL}/A_{Pb}^{HL}\right)} \left\{ \left[Z^{SD}\left(1 + \frac{A_{Pb}^{CL}}{A_{Pb}^{HL}}\right) - H^{core} \right] \rho_{Pb}^{SD} + \bar{\rho}_{Pb}^{core} H^{core} + \frac{\Delta P_{fr}^{core}}{g} \right\} . \tag{2.30}$$

Then, substituting its value into either equation in (2.26) yields the corresponding hot leg free surface level.

2.2.3 Mass balance equation

The elevation of coolant free surface levels in the hot and cold legs are calculated by imposing the conservation of mass. This fundamental principle states that mass is neither created nor destroyed, hence the change in coolant mass per unit time within a given volume can be expressed as

$$\frac{dm}{dt} = \sum \dot{m}_{in} - \sum \dot{m}_{out} , \tag{2.31}$$

in which $\dot{m}_{in}$ and $\dot{m}_{in}$ denote the sum of mass flow rates entering and exiting the volume in question. Alternatively, coolant masses in the hot leg and cold leg were previously calculated according to eq. (2.18). Then, differentiating both sides with respect to time while assuming a constant cross-sectional area yields the following equation:

$$m = A\rho Z \;\rightarrow\; \frac{dm}{dt} = AZ\frac{d\rho}{dt} + A\rho\frac{dZ}{dt} = AZ\frac{d\rho}{dT}\frac{dT}{dt} + A\rho\frac{dZ}{dt} . \tag{2.32}$$

Note that the next to last term in the above equation represents the temperature-driven expansion of the coolant. In conclusion, eqs. (2.31) and (2.32) are merely different forms of the mass balance equation, thus both expressions can be combined into

$$A\rho\frac{dZ}{dt} = \dot{m}_{in} - \dot{m}_{out} - AZ\frac{d\rho}{dT}\frac{dT}{dt} . \tag{2.33}$$

In BELLA, an extra term is added to account for the coolant transfer between the core and hot leg due to its thermal expansion. The final form of the mass balance equations as implemented in the code is

$$\begin{aligned} A_{Pb}^{HL}\rho_{Pb}^{HL}\frac{dZ^{HL}}{dt} &= \dot{m}_{Pb}^{core} - \dot{m}_{Pb}^{SG} - A_{Pb}^{HL}Z^{HL}\frac{d\rho_{Pb}}{dT}\frac{d\bar{T}_{Pb}^{HL}}{dt} - V_{Pb}^{core}\frac{d\rho_{Pb}}{dT}\frac{d\bar{T}_{Pb}^{core}}{dt} \\ A_{Pb}^{CL}\rho_{Pb}^{CL}\frac{dZ^{CL}}{dt} &= \dot{m}_{Pb}^{SG} - \dot{m}_{Pb}^{core} - A_{Pb}^{CL}Z^{CL}\frac{d\rho_{Pb}}{dT}\frac{d\bar{T}_{Pb}^{CL}}{dt} , \end{aligned} \tag{2.34}$$

where V_{Pb}^{core} is the volume of coolant in the core. Steady-state conditions are obtained by equating to zero all time derivatives, regardless of whether they involve free surface levels or temperatures. This results in the single constraint that mass flows across the core and steam generator must be equal.

2.2.4 Frictional pressure drop

The flow of fluids is always accompanied by a frictional pressure drop in the direction of flow. For an incompressible fluid, the pressure drop due to viscous effects can be characterized by the Darcy-Weisbach equation

$$\Delta P_{fr} = \left(f \frac{H}{D_h} \right) \frac{\dot{m}|\dot{m}|}{2\rho A^2} \,, \tag{2.35}$$

where the friction factor f can only be determined experimentally. Under laminar flow conditions, the friction factor is an exclusive function of the Reynolds number Re, whereas for turbulent flow it also depends on the relative roughness of the component. At Reynolds numbers greater than approximately 4000, the flow regime can be confidently assumed to be turbulent. That said, given that the Reynolds number associated with the steady-state coolant flow in the core is found around 23000, BELLA estimates the friction factor according to the Blasius correlation (Blasius, 1913),

$$f = \frac{0.316}{Re^{0.25}} \,, \tag{2.36}$$

which applies to turbulent flows at Reynolds numbers lower than 10^5. The reason behind this particular choice is the fact that, unlike other correlations available in the literature, the Blasius correlation does not contain any dependence on the relative roughness of the component. Nevertheless, frictional pressure drops calculated as in eq. (2.35) only account for distributed head losses, without taking into consideration the resistance of valves and fittings to flow.

Since the design of the reactor core includes neither valves nor deflecting fittings such as bends and elbows, flow resistance is offered solely by reducing and expanding fittings, that is, those which change the area along the fluid passageway. Given the design parameters of the hex-cans that wrap the fuel assemblies, BELLA calculates every frictional pressure drop encountered by the coolant using the formulae listed below:

$$\begin{aligned} &\text{Flow area reduction:} \quad \Delta P_{fr} = \frac{1}{2} \left(1 - \frac{A_{\text{small}}}{A_{\text{large}}} \right) \frac{\dot{m}|\dot{m}|}{2\rho A_{\text{small}}^2} \,, \\ &\text{Flow area expansion:} \quad \Delta P_{fr} = \left(1 - \frac{A_{\text{small}}}{A_{\text{large}}} \right)^2 \frac{\dot{m}|\dot{m}|}{2\rho A_{\text{small}}^2} \,, \end{aligned} \tag{2.37}$$

being A_{small} and A_{large} the flow areas on each side of the fitting. Coolant densities are evaluated at the core inlet or outlet temperatures, depending on whether the fitting in question is located before or after the fuel rod bundle.

According to the spatial solution of the neutron flux stated in eq. (2.2), the reactor power level shows a maximum at the center of the core. Consequently, requiring the same outlet temperature in all fuel assemblies implies that the mass flow rate associated with the central assembly (henceforth referred to as peak assembly) must be higher than the core-averaged value. To achieve a homogeneous temperature rise and pressure drop over the entire core, orificing is applied to the outer ring assemblies of SEALER, where the coolant mass flow rate is lower. Rather than including the effect of orifices, BELLA takes advantage of the resulting flow distribution and calculates the frictional pressure drop for the Peak Assembly (PA). Its power can be determined from the reactor power level and the radial peaking factor F_R as

$$\dot{Q}_{PA} = F_R \cdot \frac{\dot{Q}}{N} \;\rightarrow\; \dot{m}_{Pb}^{PA} = \frac{\dot{Q}_{PA}}{c_{Pb} \Delta T_{Pb}^{core}} \,, \tag{2.38}$$

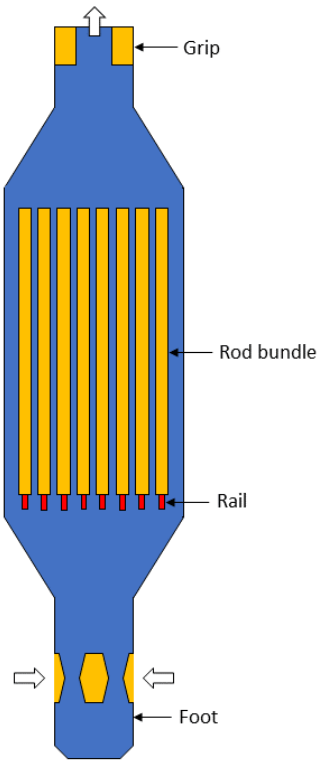

Figure 6: Schematic of an hexagonal fuel assembly duct.

where N stands for the number of fuel assemblies. Mass flow rates appearing in eqs. (2.35) and (2.37) are associated with the peak assembly and hence are calculated as shown above.

Table 2: Peak assembly frictional pressure drops at steady-state.

Rod bundle	77280 Pa
Inlet of foot	3110 Pa
Area change from foot to hexagonal section	12570 Pa
Area change from hexagonal section to rod rail section	220 Pa
Area change from rod rail section to rod bundle	3330 Pa
Area change from rod bundle to hexagonal section	5370 Pa
Area change from hexagonal to cylindrical section	170 Pa
Area change from cylindrical section to grip	380 Pa
Area change from grip to hot leg	2400 Pa
Total fuel assembly frictional pressure drop	**104840 Pa**

The steam generator of SEALER is based on the spiral heat exchanger tube design. The hot coolant is delivered from the pump into the annular plenum inside the steam generator. Then, due to the hydrostatic pressure caused by the top plate at the end of the plenum, the coolant is forced to flow radially through the spiral tube stack, transferring heat to the secondary side. The resistance offered to cross-flow by staggered layers of planar spiral tubes with diameter D and pitch P cannot be described in terms of the Darcy-Weisbach equation. Therefore, a

correlation proposed by Idelchik (1966) is used to compute the frictional pressure drop across the steam generator

$$\Delta P_{fr}^{SG} = (N_{tube}+1)\frac{\rho}{2}\left(15.6-8.35\frac{P}{D}\right)\frac{1}{r_{out}-r_{in}}\int_{r_{in}}^{r_{out}}\frac{v_{max}^2(r)}{\left[Re(v_{max}(r))\right]^{0.27}}dr\ , \tag{2.39}$$

where N_{tube} is the number of staggered layers per steam generator, r_{in} and r_{out} are the spiral initial and terminal radius respectively, and ρ is the coolant density evaluated at the average temperature of the steam generator. The Reynolds number is calculated at the maximum velocity of the coolant

$$v_{max}(r) = \frac{\dot{m}}{\rho 2\pi r h_{shell}}\frac{P}{P-D}\ , \tag{2.40}$$

where h_{shell} is the height of the spiral tube stack and $\dot{m}$ stands for the mass flow rate in a single steam generator. Note that v_{max} is a function of the spiral tube radius, hence the need for a definite integral to find the mean value of the integrand. Fortunately, an analytical expression for the frictional pressure drop in the steam generator can be obtained by substituting the above equation into eq. (2.39) and solving the definite integral, yielding

$$\Delta P_{fr}^{SG} = \frac{r_{in}^{-0.73}-r_{out}^{-0.73}}{r_{out}-r_{in}}\left(15.6-8.35\frac{P}{D}\right)\frac{N_{tube}+1}{1.46\rho}\left(\frac{\mu}{D}\right)^{0.27}\left[\frac{\dot{m}}{2\pi h_{shell}}\frac{P}{P-D}\right]^{1.73}\ , \tag{2.41}$$

in which μ is the coolant viscosity evaluated at the average temperature of the steam generator.

2.3 Decay heat

The removal of decay heat is a major reactor safety concern, in particular shortly after a reactor SCRAM or following the onset of a ULOHS transient. In view of this reality, the current version of BELLA incorporates the capability to estimate the decay heat resulting from radioactive decay of unstable fission products. The model is based on the 1994 American National Standard (ANS) for decay heat power in LWRs (American Nuclear Society, 1994). It provides exponential decay curves derived from experimental data acquired for three isotopes: ^{235}U, ^{238}U and ^{239}Pu. However, several simplifications are made since the purpose of the decay heat module is to yield a rough estimation, rather than a precise calculation.

First, BELLA neglects the contribution of minor actinides to decay heat, as their activity only becomes relevant for longer decay times ($>10^4$ s) (American Nuclear Society, 1994). Furthermore, the model does not account for the heat source that arises from fission products undergoing neutron capture reactions after the reactor has been shut down. Finally, the 1994 ANS report does not contain any information on decay heat fractions for fast reactors owing to the fact that it was originally developed for LWR designs. In the absence of experimental data specific to fast fission, BELLA adopts the decay curves provided for thermal fission of the most abundant fissile material in the fuel, that is, ^{235}U. Note that the amount of inaccuracy introduced by using thermal fission data far exceeds the error resulting from not considering ^{238}U and ^{239}Pu. Therefore, the decay heat model as implemented in the code is limited to ^{235}U, henceforth referred to as decay heat precursor.

By convention, the ANS uses 23 groups to describe each decay heat precursor. On this basis, the work of Paulsen et al. (2014) was used as a guide in writing the equations describing decay heat, which are analogous to those for the delayed neutron precursors

$$\frac{dh_j(t)}{dt} = \frac{\beta_j}{\varepsilon_{fiss}}n(t) - \lambda_j h_j(t)\ \ ;\ \ j=1,...,23\ , \tag{2.42}$$

where h_j is defined as the decay heat power released by group j relative to the power generated from fission under steady-state conditions. Recall that $n(t)$ refers to the normalized, time-dependent neutron population. The parameters β_j (in units of MeV/s) and λ_j are respectively the decay power fraction and the decay constant for group j. Both are obtained from the ANS. Lastly, ε_{fiss} is the energy released per fission event in units of MeV, which averages around 200 MeV for ^{235}U. The solution to the above equation at steady-state is

$$h_j(0) = \frac{\beta_j}{\varepsilon_{fiss}\lambda_j} \, . \tag{2.43}$$

Bearing in mind the initial condition for the time-dependent neutron population $n(0) = 1$, eq. (2.3) can be re-written to include the heat source resulting from the decay of ^{235}U fission products, hence obtaining the total thermal power

$$\dot{Q}_{th}(t) = \dot{Q}(0)n(t) + \dot{Q}(0)\sum_{j=1}^{23} h_j(t) \, . \tag{2.44}$$

3 New fuel thermo-mechanical model

The BELLA reference model does not take into consideration the thermo-mechanical evolution of the fuel and cladding during irradiation. This chapter is devoted to modelling the most important mechanisms and processes affecting fuel properties and behaviour, including temperature, irradiation, and fission product effects.

3.1 Thermal expansion of the fuel and cladding

Prior to running any transient calculation, the fuel rod design parameters - fuel pellet diameter, cladding outer diameter, and cladding thickness - must be defined through the BELLA input file at the so-called hot state, that is, nominal operating conditions. Although these parameters remain constant during transient simulations performed with the reference BELLA code, in reality, solid materials tend to change their geometry in response to temperature variations. This thermal expansion results from an increase in the kinetic energy of the individual atoms in the crystal lattice when heat is applied. As atoms oscillate near their equilibrium positions with larger amplitudes, the average atomic spacing increases and the solid expands. Thermal expansion is mainly a function of the lattice energy of the crystalline solid, thus generally decreasing as the strength of the bond increases.

The coefficient of linear thermal expansion α describes the relative expansion of a material body along a particular direction per degree change in temperature

$$\alpha(T) = \frac{1}{L}\frac{dL}{dT} \,, \tag{3.1}$$

where L refers to a particular length measurement. It depends on the material and varies with temperature. Integrating the above expression between two arbitrary temperatures T_1 and T_2 yields

$$\frac{L(T_2)}{L(T_1)} = \exp\left(\int_{T_1}^{T_2} \alpha(T)dT\right) \simeq 1 + \int_{T_1}^{T_2} \alpha(T)dT \,, \tag{3.2}$$

where the latter approximation is accurate enough provided that the definite integral is evaluated over a sufficiently narrow interval of temperatures, meaning that the exponential function can be approximated as its first-order Taylor polynomial.

Following the onset of a power transient, the oxide fuel temperature increases rapidly. The combination of rising temperatures and their associated thermal gradients may have far-reaching consequences for the pellet geometry and its microstructure. Among the geometric effects resulting solely from temperature, thermal expansion is known to be a limiting factor for the lifetime of the fuel in the reactor. It entails dimensional changes in the fuel pellet and cladding surfaces, thereby contributing to fuel-cladding mechanical interaction. Despite the cladding material (15-15Ti) having a larger coefficient of thermal expansion as compared to the oxide fuel (Figure 7), the thermal expansion of the latter is always greater in absolute terms because of exposure to much higher temperatures throughout the transient. Altogether this leads to a net reduction of the gap thickness.

The relatively poor thermal conductivity of oxide fuels results in a steep temperature gradient along the radial direction, which prompts a differential thermal expansion of the fuel pellet; its centre tends to expand more than the periphery. At temperatures below half the melting

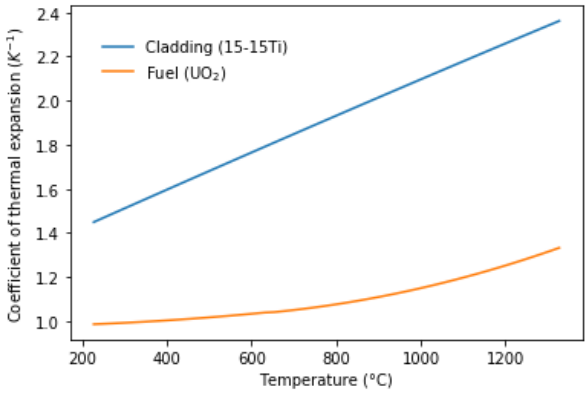

Figure 7: Coefficient of linear thermal expansion for fuel and cladding materials.

point, most ceramic fuels exhibit a brittle mechanical behaviour (Bailly et al., 1999). Therefore, under these conditions, circumferential stresses may eventually induce radial cracking. Pellet cracking is highly detrimental to nuclear fuel performance and limits its high-burnup operation. If, for example, a crack grows sufficiently to intersect a free surface, the release of gaseous fission products into the gap will be accelerated. Moreover, corrosive fission products transported through these cracks may induce stress corrosion cracking in the cladding, degrading its structural integrity. This phenomenon is further aggravated as the gap thickness decreases and the fuel gets into contact with the inner surface of the cladding.

The new thermo-mechanical model as implemented in BELLA recalculates the fuel pellet diameter, cladding inner diameter, and cladding outer diameter at every simulation time step based on eq. (3.2). It is important to highlight that the dimensional change in the fuel pellet diameter is estimated from its average temperature, thereby not considering the differential thermal expansion caused by the temperature gradient.

3.2 Thermal conductivity of oxide fuels

Thermal conductivity is defined as the rate of heat transfer by conduction through a unit cross-section area of a material. It is one of the most important design parameters of a nuclear fuel element since it directly determines the temperature gradient between the surface and the centreline of the pellet. A higher thermal conductivity leads to an improved margin to fuel melting, thus allowing for operation at higher power densities and ultimately decreasing the overall cost of electricity. Having said that, even though conventional oxide fuels have a substantially lower thermal conductivity as compared to advanced nuclear fuels (metal alloys, nitrides, and carbides), they are chemically stable, inexpensive to manufacture, and have a very high melting point (2847 ºC).

Thermal conductivity of oxide fuels depends on a considerable number of parameters: temperature, fuel composition, porosity (p), oxygen-to-metal (O/M) ratio or deviation from stoichiometry (x), and burnup (BU), some of which are interrelated. Note that fuel composition refers to the plutonium content in the case of MOX fuels. As for unirradiated, 100% dense, oxide fuels (that is $p = 0$, BU $= 0$), their thermal conductivity λ_0 can be written as a function of temperature and deviation from stoichiometry. The correlation implemented in BELLA consists of two terms, corresponding to the phononic (or lattice) and electronic thermal con-

ductivity respectively

$$\lambda_0(x,T) = \frac{1.1579}{A(x)+B(x)T} + \frac{2.3434\cdot 10^{11}}{T^{5/2}} \exp\left(-\frac{16350}{T}\right), \tag{3.3}$$

where T is the temperature in Kelvin in the range of $700 \leq T \leq 3100$ K and

$$\begin{aligned} A(x) &= 2.85x + 0.035 \\ B(x) &= (2.86 - 7.15x)\cdot 10^{-4}\,. \end{aligned} \tag{3.4}$$

As its name indicates, the phononic term describes the contribution of phonons, that is, collective excitations of atoms in the crystal lattice, and its formulation is based on experimental data by Duriez et al. (2000). Following a temperature rise, the amplitude of atomic vibrations increases, thus contributing to a larger interference with phonon transport. This entails a higher resistance to heat transfer, which translates into a lower thermal conductivity. The parameter A in the above expression is related to the scattering of phonons by imperfections in the lattice, such as dissolved fission products, whereas the parameter B accounts for scattering processes through phonon-phonon interaction. On the other hand, the electronic contribution becomes dominant at high temperatures ($T > 2000\ K$), meaning that heat conduction is accomplished essentially by the transport of free electrons. The expression for the electronic thermal conductivity was obtained from the analysis carried out by Ronchi et al. (1999).

The reference BELLA code uses eq. (3.3) to compute the thermal conductivity at the interface of two adjacent fuel nodes, thereby neglecting the effects of porosity and irradiation. To improve the accuracy of simulations under normal and accident conditions, the new thermomechanical model includes a comprehensive approach to modelling the thermal conductivity of irradiated UO_2 fuel based on the work of Lucuta et al. (1996). Each effect envisaged in the new model can be added as a correction factor to the expression for the thermal conductivity of unirradiated, 100% dense, oxide fuel, yielding

$$\lambda(x,T,p,\mathrm{BU}) = \lambda_0(x,T)\cdot\kappa_{\mathrm{P}}(p)\cdot\kappa_{\mathrm{DFP}}(T,\mathrm{BU})\cdot\kappa_{\mathrm{PFP}}(T,\mathrm{BU})\cdot\kappa_{\mathrm{RD}}(T) \tag{3.5}$$

where κ_{P} describes the effect of porosity, including the formation of fission gas bubbles, and κ_{DFP}, κ_{PFP} and κ_{RD} describe the variations in thermal conductivity due to dissolved fission products, precipitated fission products and radiation damage respectively. Henceforth, temperatures are given in Kelvin and burnup is expressed in units of atomic percent (at. %), that is, the number of atoms that underwent fission relative to the initial amount of metal atoms.

3.2.1 Effect of porosity

The effective thermal conductivity of oxide fuels decreases with porosity since the rate of heat transfer through gas-filled pores is much lower than through the crystalline lattice. As burnup advances, gaseous fission products accumulate and coalesce into bubbles, potentially leading to an increase in the centreline temperature of the fuel element. Extensive experimental studies show that the effect of fuel porosity on thermal conductivity strongly depends on the morphology and orientation of the pores (Bailly et al., 1999). Fission gas bubbles formed in the grains (intragranular) typically have a near-spherical shape and a size comparable to the phonon mean free path. Therefore, intragranular bubbles favour phonon scattering in a similar vein to dissolved fission products, causing a reduction in the phononic conductivity. Large bubbles formed at the grain boundaries (intergranular), usually in the form of elongated pores

or microcracks, entail a greater detriment for thermal conductivity than spherical and regularly distributed pores. For this reason, intergranular bubbles constitute a more significant impediment to heat transfer in the fuel pellet.

In addition to the porosity arising from irradiation via fission gas-bubbles formation, a moderate amount of porosity (5-10%) is introduced to oxide fuels during the fabrication process. This is done precisely to permit the accommodation of such gaseous products. The degree of complexity associated with reproducing the evolution of irradiation-induced porosity throughout the entire life of the reactor extends beyond the scope of this thesis. Thus, the new thermo-mechanical model is limited to modelling the effect of fabricated porosity. Its value is defined by the user through the BELLA input file. The Maxwell-Eucken relation can be applied for porosities below 20% (Winter and MacInnes, 1988)

$$\kappa_{\mathrm{P}} = \frac{1-p}{1+(\gamma-1)p} \approx \frac{1-p}{1+p}\,, \tag{3.6}$$

where γ is a pore shape factor and p includes the single contribution from fabricated porosity. For simplicity, a mean value of $\gamma = 2$ is adopted for the shape factor in BELLA, bearing in mind that its value equals 1.5 in the case of spherical pores and increases as they become more elongated. Note that the mass density of 100% dense oxide fuel ρ_{100} must be modified to account for porosity

$$\rho_{100} \;\rightarrow\; \rho = \rho_{100}\,(1-p)\,. \tag{3.7}$$

3.2.2 Effect of solid fission products

Most fission products form solid phases within the fuel, affecting its thermal conductivity by causing variations in the phononic contribution. Depending on the type of phase formed, solid fission products can be classified as:

- Dissolved in the fuel matrix as oxides: Sr, Zr, Nb, Y, La, Ce, Pr, Nd, Pm, Sm.
- Forming metallic precipitates: Mo, Tc, Ru, Rh, Pd, Ag, Cd, In, Sn, Sb, Te.
- Forming oxide precipitates: Rb, Cs, Ba, Zr, Nb, Mo, Te.

Oxidized fission products in solution introduce additional scattering centers into the fuel matrix, further interfering with phonon transport. Consequently, their presence causes a reduction in the thermal conductivity of the fuel. The effect of dissolved fission products is described in terms of a factor proposed by Lucuta et al. (1996) which depends on temperature and burnup as

$$\kappa_{\mathrm{DFP}} = \left[C(\mathrm{BU}) + D(\mathrm{BU})\sqrt{T}\right] \arctan\left[\frac{1}{C(\mathrm{BU}) + D(\mathrm{BU})\sqrt{T}}\right]. \tag{3.8}$$

The temperature dependence reflects the fact that the solubilities of the oxidized fission products depend on temperature. The parameters C and D are expressed as a function of burnup

$$\begin{aligned} C(\mathrm{BU}) &= \frac{1.09}{\mathrm{BU}^{3.265}} \\ D(\mathrm{BU}) &= \frac{0.0643}{\mathrm{BU}^{0.5}}\,. \end{aligned} \tag{3.9}$$

On the contrary, fission products forming metallic inclusions contribute positively to thermal conductivity due to their superior ability to conduct heat as compared to the oxide fuel matrix. The size of these precipitates is strongly dependent on the temperature, ranging between 0.05 and 1 μm in diameter (Lucuta et al., 1996). Nevertheless, a micrographic examination of highly irradiated fuel in fast reactors reveals that some metallic precipitates migrate to the high-temperature region of the fuel pellet, forming clusters with a considerable diameter of up to 1 mm (Bailly et al., 1999). In the range from 600 to 1900 K, the effect of precipitated fission products is taken into account by introducing yet another factor

$$\kappa_{\mathrm{PFP}} = 1 + \frac{0.019\ \mathrm{BU}}{3 - 0.019\ \mathrm{BU}} \left[1 + \exp\left(-\frac{T - 1200}{100} \right) \right]^{-1} . \tag{3.10}$$

To account for the fact that the precipitation of metal fission products is not uniform along the radial direction of the fuel pellet, but rather concentrated around its centreline, the above factor contains an exponential function with a transition height at 1200 K. As a result, at temperatures below this threshold, the contribution of precipitates to the thermal conductivity of the fuel can be neglected.

3.2.3 Effect of radiation damage

Radiation damage results mainly from the constant bombarding of neutrons and the alpha-decay of actinides. Vacancies and self-interstitial defects are created when the incident radiation is sufficiently energetic to displace atoms from their equilibrium positions in the crystal lattice, leading to a significant energy build-up. Such defects interfere with phonon transport, thus causing a reduction in the phononic contribution to thermal conductivity. However, as temperature increases, vacancies and interstitial defects might recombine to restore the equilibrium structure, meaning that radiation damage decreases as recombination mechanisms become thermally activated. Its influence on thermal conductivity is quantified based on the formula suggested by Lucuta et al. (1996)

$$\kappa_{\mathrm{RD}} = 1 - 0.2 \left[1 + \exp\left(\frac{T - 900}{80} \right) \right]^{-1} . \tag{3.11}$$

At low temperatures, all the damage is stored in the lattice and radiation damage is greater. Oxygen defects anneal by recombination already below fuel operating temperatures. Therefore, the damage induced to the oxygen sub-lattice is not taken into consideration in the above expression. On the other hand, uranium defects are known to recombine at temperatures around 1000 K, meaning that most changes in thermal conductivity are observed below such threshold. For this reason, the radiation damage factor includes an exponential function with a transition height at 900 K.

3.3 Fission gas release

The behaviour of gaseous products introduced by the fission of uranium and plutonium atoms is discussed in this subsection. In both thermal and fast reactors, this includes primarily noble gases, namely xenon, krypton, and helium. The production of helium results mainly from alpha-decay processes occurring within the transmutation chain of several actinides such as

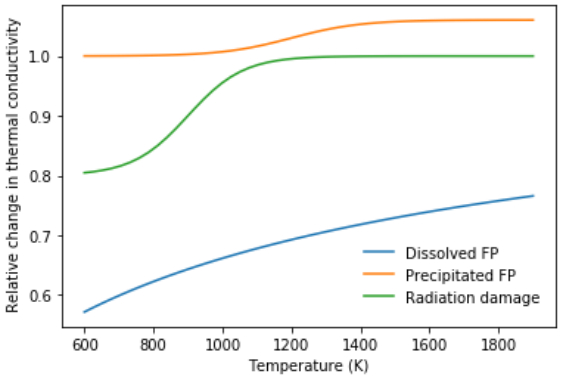

Figure 8: Relative change in thermal conductivity of UO_2 fuel due to irradiation effects at 9% burnup.

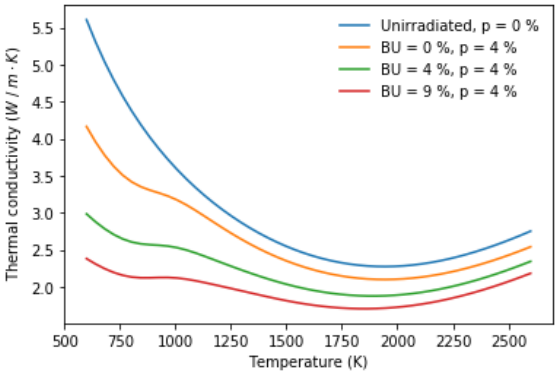

Figure 9: Thermal conductivity of UO_2 as a function of temperature.

^{238}Pu, ^{241}Am, and ^{242}Cm. To a lesser extent, helium is created as a byproduct of ternary fission as well as from neutron capture by oxygen atoms in the fuel matrix. The fission yield of these noble gases is sensitive to the nature of the fissile atom, the neutron flux spectrum, and the burnup. However, in fast reactors, each fission event produces on average 0.23 xenon atoms, 0.02 krypton atoms, and 0.01 helium atoms (Bailly et al., 1999). The fact that noble gases have a tendency for non-reactivity translates into a very low solubility in the crystal lattice. As a result, three life-limiting phenomena arise in the fuel element:

- Swelling of the fuel
- Fission gas bubble formation (Irradiation-induced porosity)
- Fission gas release into the fuel-cladding gap

In the first two cases, gaseous fission products remain in the fuel pellet. Fuel swelling is defined as the positive change in fuel volume resulting from an increasing number of atoms generated by fission. A more detailed description of the oxide fuel swelling is provided in subsection 3.4. For the moment, it is sufficient to know that its most significant impact on fuel performance is due to the closing of the gap, which leads to a pressure build-up and, eventually, to fuel-cladding mechanical interaction. As for fission gas bubbles, their effect was already discussed in subsection 3.2.1, arguing that irradiation-induced pores play a role similar to that of fabricated porosity due to their intrinsically low thermal conductivity. Therefore, this phenomenon entails a reduction in the overall heat transfer capability of the fuel pellet.

Fission gas release into the open gap results in a decrease of its effective heat transfer coefficient. This is because of the considerably lower thermal conductivity of xenon and krypton in comparison with helium. Poorer heat conduction between fuel and cladding leads to higher fuel temperatures, which further enhance gas release, thereby giving rise to a positive feedback. At the same time, the accumulation of fission gases in the fuel rod plenum prompts a pressure build-up that may eventually compromise the integrity of the fuel element. The basic mechanisms involved in the fission gas release are described below.

3.3.1 Athermal mechanisms

The fission of a uranium or plutonium atom into lighter nuclei is accompanied by an energy release of about 200 MeV. Even though the outcome of an individual fission event is not predictable, on average 168 MeV are transformed into kinetic energy of the fission products. Most of this energy is dissipated through collisions with the atoms in the crystal lattice, that is, uranium and oxygen in the case of UO_2. Statistically, highly-ionized fission fragments travel a distance of about 8 μm before being brought to rest (Bailly et al., 1999). With this information, it is clear that those fission products born sufficiently close to the free surface of the fuel pellet have a higher probability of escaping into the fuel-cladding gap. This mechanism is called fission gas release by direct recoil. It is proportional to the fission rate, the range of the fission fragment, and influenced by the geometry of the fuel pellet. However, the direct-recoil release is independent of temperature, therefore considered an athermal mechanism.

Along the path towards the fuel pellet boundary, those fission products with enough kinetic energy may displace the atoms contained in a certain volume near the point of exit. Stationary gas atoms that are sufficiently close to the surface may be ejected as a result of the interaction with a fission fragment. This mechanism is referred to as fission gas release by knock-out. Furthermore, fission fragments travelling through the oxide fuel lose their kinetic energy at an approximate rate of 10 keV/nm. Consequently, a high local heat pulse appears along their pathway. Should this occur in the vicinity of the free surface of the fuel, the heated zone as a whole may be sputtered, including the gaseous fission products contained within its volume.

Both knock-out and sputtering processes are athermal mechanisms. Unlike direct-recoil release, however, their respective release rates are inversely proportional to the radioactive decay constant of the isotopes to be ejected. In other words, the longer the half-life of a particular isotope at rest near the free surface, the higher the probability of being drawn towards the exterior through the interaction with a newly born, thus highly-energetic, fission product. Finally, as the number of gas atoms in the fuel pellet increases with burnup, the fraction of gas released by knock-out and sputtering must therefore increase as well.

Direct-recoil, knock-out, and sputtering mechanisms play a dominant role in the release of gaseous fission products at fuel temperatures below 1000 ºC. Under these conditions, diffusion is enhanced as a result of the fission process (recoil-assisted diffusion) rather than being driven by temperature (thermal diffusion). In PWR pellets irradiated to a burnup of 45 MWd/kgU, for example, the fraction of athermal fission gas release is slightly below 1%, whereas at 60 MWd/kgU its value increases to roughly 3% (Van Uffelen, 2006).

3.3.2 Thermally activated mechanisms

Observation on the microstructure of oxide fuel pellets irradiated at high power and burnup reveals a central zone characterized by the presence of intragranular pores and the interconnection of bubbles at the grain boundaries. However, a lack of xenon and other volatile elements is observed in such central zone, indicating that gaseous fission products have already been released (Tourasse et al., 1992). In addition to these findings, the fact the periphery of the fuel pellet retained the totality of these gases suggests the existence of a temperature threshold that determines the onset of a nearly total fission gas release. Its parametrization as a function of

burnup is known in the literature as the Vitanza threshold (Van Uffelen, 2006)

$$T = \frac{9800}{\ln\left(200\ \mathrm{BU}\right)}\ , \tag{3.12}$$

where temperature is given in degrees Celsius and burnup is given in units of $\mathrm{MWd/kgUO_2}$.

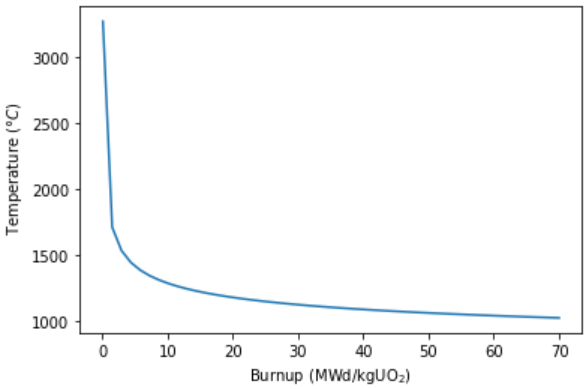

Figure 10: Vitanza threshold for the onset of total fission gas release.

The appearance of such a sudden fission gas release over a certain temperature threshold and its dependence on burnup can be qualitatively justified by considering the role of thermally activated mechanisms. From the very beginning of irradiation, gas atoms are introduced into the lattice as a result of fission reactions. Diffusion within the crystal lattice of the oxide fuel occurs by either interstitial or substitutional mechanisms. In the first case, gas atoms migrate by forcing their way between solution sites in the lattice structure, whereas in the second case, their motion is conditioned to the existence of an unoccupied site (vacancy) at one of the adjacent lattice positions. As explained in subsection 3.3.1, the contribution from highly-energetic fission fragments dominates the diffusion rate of gas atoms at temperatures below 1000 ºC. In an intermediate temperature range from 1000 ºC to 1400 ºC, point vacancies necessary for substitutional lattice diffusion are created due to the effects of both temperature and radiation damage induced by fission fragments. Above 1400 ºC, thermally activated mechanisms play a predominant role and the contribution from athermal mechanisms can be neglected.

At temperatures higher than 1400 ºC, intragranular bubbles migrate to the grain boundaries either in a stochastic manner under the effect of the thermal gradient, increasing their average size as they coalesce with others. After a certain degree of burnup, this migration results in the accumulation of fission gas bubbles along grain boundaries, owing to the fact that these regions are energetically more favourable. Its most immediate consequence is the swelling of the fuel, which in the case of fast reactors would be enormous if the larger fraction of the gas was not released into the gap. Then, the interconnection of several intergranular bubbles leads to the development of a so-called grain edge tunnel, that is, a microstructure resembling a tunnel network that allows for rapid transport of gaseous fission products. Eventually, grain edge tunnels grow large enough to reach a free surface, thereby releasing all the accumulated intergranular gas into the fuel-cladding gap, and subsequently to the gas plenum.

Prior to the formation of a continuous network of grain edge tunnels extending to the outer surface of the fuel, the release rate of gaseous fission products is mostly driven by athermal

mechanisms, hence remains small. This incubation period, during which 99% of the gas produced is retained within the fuel pellet, corresponds roughly to the Vitanza threshold. For a given burnup, an instantaneous 100% release into the free volume of the fuel rod is assumed above the temperature threshold defined in eq. (3.12).

3.3.3 Implementation in BELLA

For simplicity, the fission gas release model implemented in BELLA is limited to the release of xenon, thus neglecting the contributions from krypton and helium. The choice made was based on the fact that the average fission yield of xenon in fast reactors ($Y_{\text{Xe}} = 0.23$ atoms/fiss) is an order of magnitude greater than that of the other noble gases ($Y_{\text{Kr}} = 0.02$ atoms/fiss). That said, the first step consists of computing the number of xenon atoms born from fission as a function of burnup. Given the power generated from fission $\dot{Q}$ and the amount of energy released per fission event ε_{fiss}, the number of xenon atoms born per second is

$$\dot{B}_{\text{Xe}} = \frac{Y_{\text{Xe}}\,\dot{Q}}{\varepsilon_{fiss}}\,, \tag{3.13}$$

where ε_{fiss} was estimated at 200 MeV, corresponding roughly to ^{235}U, even though its actual value depends on the fissioning nuclide. Note that the factors in the above equation must ensure that $\dot{B}_{\text{Xe}}$ is expressed in units of s^{-1}. Next, the elapsed time from the start-up of the reactor ($t = 0$) to the point in life where the transient simulation is performed ($t = T$) can be computed from the definition of burnup, that is, the energy released from fission per initial mass of fuel

$$\text{BU} = \frac{\int_0^T \dot{Q}(t)\,dt}{m_0} \approx \frac{\dot{Q}\,T}{m_0} \;\rightarrow\; T = \frac{m_0\,\text{BU}}{\dot{Q}}\,, \tag{3.14}$$

where m_0 refers to the initial mass of fuel. Burnup must be expressed in units of MWd/kgU or similar, thus needs to be converted from atomic percent. The conversion factor requires knowledge of the energy released per fission event. With the value presented above, BELLA approximates 100% burnup as 937.5 MWd/kgU. Since the power level history before the beginning of the transient simulation is not known, BELLA assumes that the reactor operated continuously at 100% power under steady-state conditions. Then, combining eqs. (3.13) and (3.14) yields the number of xenon atoms born during the elapsed time T

$$B_{\text{Xe}}(T) = \dot{B}_{\text{Xe}}\,T = \frac{Y_{\text{Xe}}\,m_0\,\text{BU}}{\varepsilon_{fiss}}\,. \tag{3.15}$$

Finally, the number of xenon atoms born from the start-up of the reactor to any time step in the transient calculation is computed as

$$B_{\text{Xe}}(t) = \frac{Y_{\text{Xe}}}{\varepsilon_{fiss}}\left(m_0\,\text{BU} + \int_0^t \dot{Q}(t')\,dt'\right)\,. \tag{3.16}$$

Fission gas release is modelled independently for each radial zone - central, middle, outer - in the fuel pellet. The Vitanza threshold can easily be computed at the start of the simulation from the degree of burnup, then remains constant during the transient calculation. At the end of every simulation time step, fuel temperatures obtained by solving the energy balance equations are compared to the Vitanza threshold. The outcome of each comparison determines whether the fission gas release from each particular radial zone is partial or total, which is reflected in the release-to-birth ratio R/B.

Assuming that under steady-state conditions none of the fuel pins in the SEALER core achieves temperatures higher than 1000 ºC, thereby remaining below the Vitanza threshold, the release-to-birth ratio of xenon is estimated at 1% throughout the entire prior history of the reactor. This is in accordance with the fact that in the temperature range where recoil-assisted diffusion dominates over thermal diffusion, the fuel pellet is capable of retaining about 99% of the gaseous fission products. By applying this ratio to the quantity calculated in eq. (3.16), the number of xenon atoms released into the fuel-cladding gap from the *i*-th radial zone can be written as a function of the simulation time

$$R_{\mathrm{Xe},i}(t) = \frac{Y_{\mathrm{Xe}}}{\varepsilon_{fiss}} \left(m_{0,i}\ \mathrm{BU} \left(\frac{R}{B}\right)_{0,i} + \left(\frac{R}{B}\right)_{i}(t) \int_0^t \dot{Q}_i(t')\, dt' \right) , \tag{3.17}$$

where $m_{0,i}$ and $\dot{Q}_i$ denote respectively the fuel mass and fission power level associated with the *i*-th radial zone, $(R/B)_{0,i}$ is the steady-state release-to-birth ratio and $(R/B)_i$ is a step function which equates to 1% while the fuel temperature of the *i*-th radial zone lies below the Vitanza threshold. Otherwise, a total fission gas release is assumed, thus the time-dependant release-to-birth ratio becomes 100%. The total number of xenon atoms released throughout the entire life of the reactor up to a given simulation time is obtained by adding the contribution from the three radial zones of the fuel

$$N_{\mathrm{Xe}}(t) = R_{\mathrm{Xe},ctr}(t) + R_{\mathrm{Xe},mid}(t) + R_{\mathrm{Xe},out}(t)\ . \tag{3.18}$$

As xenon is released into the fuel rod free volume, the thermal conductivity of the gap decreases, leading to poorer heat conduction between the fuel and cladding. This is due to the fact that xenon has a significantly lower thermal conductivity as compared to helium. The reference BELLA code uses a simplified model where the gap is filled with pure helium gas. Therefore, its effective heat transfer coefficient can be calculated directly from the thermal conductivity of helium. However, the new thermo-mechanical model includes a mixture of helium and xenon. Its composition can be described at any time by the atomic fractions of the gases. Helium is introduced into the fuel element at atmospheric pressure and room temperature during the fabrication process. Note that the volume available to accommodate the gas V includes both the fuel-cladding gap and the plenum above the fuel column. Then, the number of helium atoms in the mixture is calculated from the ideal gas law

$$PV = n_{\mathrm{He}} \Re T \ \rightarrow\ N_{\mathrm{He}} = n_{\mathrm{He}} N_A = \frac{PV N_A}{\Re T}\ , \tag{3.19}$$

where $\Re$ is the universal gas constant, n_{He} and N_{He} are the number of moles and atoms of helium respectively, and N_A is the Avogadro constant. Recalling the result obtained for xenon in eq. (3.18), the atomic fraction of pure gas for component i is calculated as

$$\chi_i = \frac{N_i}{N_{\mathrm{He}} + N_{\mathrm{Xe}}}\ . \tag{3.20}$$

Finally, BELLA estimates the thermal conductivity of the helium-xenon mixture (Figure 11) using a formula derived from the kinetic theory of gases (Cahalan et al., 2012)

$$\lambda_{\mathrm{He,Xe}} = \frac{\lambda_{\mathrm{He}}}{1 + G_{\mathrm{He,Xe}} \dfrac{\chi_{\mathrm{Xe}}}{\chi_{\mathrm{He}}}} + \frac{\lambda_{\mathrm{Xe}}}{1 + G_{\mathrm{Xe,He}} \dfrac{\chi_{\mathrm{He}}}{\chi_{\mathrm{Xe}}}}\ . \tag{3.21}$$

This value replaces the former thermal conductivity of helium used to calculate the gap conductance term in the reference BELLA code. The coefficient G_{ij} can be interpreted as the ratio of efficiencies with which atoms of j and i respectively impede the conduction of heat by atoms of i.

$$G_{ij} = \frac{1.065}{\sqrt{8}} \left(1 + \frac{M_i}{M_j}\right)^{-1/2} \left[1 + \left(\frac{\lambda_i}{\lambda_j}\right)^{1/2} \left(\frac{M_i}{M_j}\right)^{1/4}\right]^2 . \tag{3.22}$$

where M is the atomic weight.

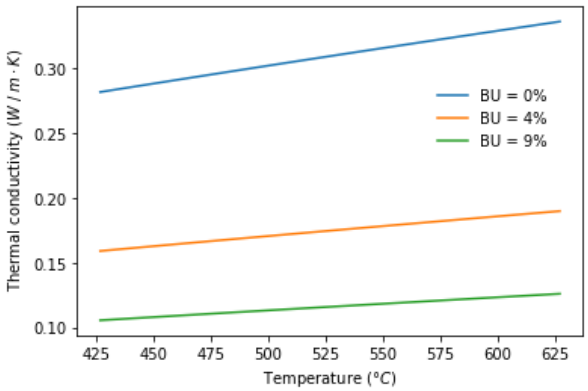

Figure 11: Thermal conductivity of the He-Xe mixture as a function of temperature.

3.4 Swelling of the fuel

Fuel swelling is defined as the positive change in fuel volume induced by the accumulation of fission products during irradiation. It is driven mainly by two factors: the evolution of the lattice parameter of the oxide due to the presence of solid fission products dissolved in the matrix and the formation of fission gas bubbles with intrinsically low solubility. Except for lanthanum and caesium, all the other soluble fission products induce a contraction of the lattice as they replace a heavy atom. The net contribution of solid fission products to fuel swelling is thus a negative change in volume. Nevertheless, the most significant effect is due to gaseous fission products coalescing into bubbles and diffusing along grain boundaries. Therefore, the total volume change resulting from fuel swelling is always positive.

Admittedly, gaseous swelling of the fuel is heavily linked to the topic of fission gas release described in subsection 3.3. In fact, it is often argued that fuel swelling is the step prior to a total fission gas release rather than an individual physical process. In the present work, however, these phenomena are separated into two different subsections. This can be justified on the grounds that density measurements carried out on oxide fuel after irradiation in a fast reactor reveal a constant swelling rate as burnup increases (Pascard, 1985). More specifically, it was observed that the density of oxide fuel pellets can be described by a linear function of burnup with a swelling rate of 0.62% per percent burnup

$$\rho(\text{BU})\ [\text{kg/m}^3] = \rho_{100}\ [\text{kg/m}^3]\ \left(1 - 0.0062 \cdot \text{BU}\ [\text{at \%}]\right) . \tag{3.23}$$

Experimental data shows that the above correlation applies at burnup values as high as 20%. Having a constant swelling rate right up to such a high degree of burnup leads to the conclusion that fuel swelling can be quantified regardless of the onset of fission gas release. Despite

the fact that oxide pellets irradiated in fast reactors have been observed to release their entire production of gaseous fission products around 7-8% burnup, the onset of such release does not seem to influence the swelling rate according to density measurements (Pascard, 1985).

The implementation of fuel swelling in BELLA consists of redefining the fuel pellet radius before launching any transient calculation given its value at beginning-of-life (BOL) and the level of burnup. The user is required to manually input both parameters through the BELLA input file. Then, the pellet radius can be estimated from the burnup-dependent density of the oxide fuel as stated in eq. (3.23)

$$\frac{\rho_{\text{BOL}}}{\rho(\text{BU})} \approx \frac{R(\text{BU})^2}{R_{\text{BOL}}^2} \;\rightarrow\; R(\text{BU}) = R_{\text{BOL}}\sqrt{\frac{\rho_{\text{BOL}}}{\rho(\text{BU})}}\,, \tag{3.24}$$

where two approximations have been made: the height of the fuel column and the total mass of fuel in the core are assumed to remain constant throughout the entire life of the reactor. The latter can be justified based on the definition of burnup.

$$\text{BU} = \frac{E_{fiss}}{m_0} = \frac{\Delta m\, c^2}{m_0} \;\rightarrow\; \frac{m(\text{BU})}{m_0} = \frac{m_0 - \Delta m}{m_0} = 1 - \frac{\text{BU}}{c^2} \approx 1\,, \tag{3.25}$$

in which E_{fiss} is the amount of fission-energy extracted from the initial mass of fuel, Δm is the cumulative mass defect resulting from all the atoms that underwent fission, and c is the speed of light.

3.4.1 Solid-to-solid heat transfer

The radius of the fuel pellet increases according to eq. (3.24) as burnup advances towards EOL, whereas the inner radius of the cladding remains unchanged. As a result, the fuel-cladding gap decreases until it eventually disappears. Given the fuel rod design parameters of SEALER, Figure 12 displays the thickness of the gap as a function of burnup. Note that the thermal expansion of the fuel and cladding is not taken into consideration. The gap closure generated by the swelling of the fuel utterly invalidates the heat transfer model implemented in the reference BELLA code. In particular, having a null or negative gap thickness leads to a math domain error in the heat transfer coefficient stated in eq. (2.11). In this light, a new formulation must be introduced.

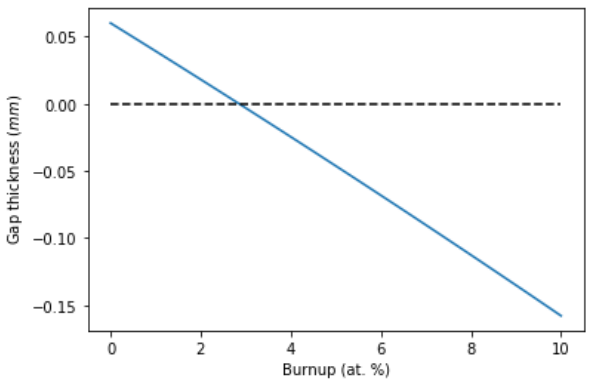

Figure 12: Fuel-cladding gap thickness as a function of burnup.

The reference BELLA code successfully models heat conduction between the outer surface of the pellet and the inner wall of the cladding provided that the gap remains open. Once closure occurs, however, heat is passed directly through solid-to-solid contact rather than through a gas-filled gap. In addition, the new thermo-mechanical model assumes that the fuel pellet cannot expand further once it comes into contact with the inner cladding wall. Consequently, if the outcome of eq. (3.24) implies a negative gap thickness, the fuel pellet radius is set equal to the inner cladding radius regardless of the burnup. Thereafter, the solid-to-solid heat transfer coefficient h_{ss} in units of W/K is formulated in terms of the correlation suggested by Lassmann and Pazdera (1983)

$$h_{ss} = 2\pi R \mathbb{H} n \frac{A \lambda_{\text{eff}}}{\Psi^{2m-1}} \left(\frac{P_i}{\Pi} \right)^m , \tag{3.26}$$

where A and m are correlation parameters determined experimentally, P_i and λ_{eff} are the fuel-cladding interface pressure and effective thermal conductivity respectively, Π is the hardness of the cladding in units of Pa, and Ψ is the root-mean-square of the roughness defined from the individual surface roughnesses of the fuel ξ_f and cladding ξ_c as

$$\Psi = \sqrt{\frac{\xi_f^2 + \xi_c^2}{2}} . \tag{3.27}$$

The effective thermal conductivity is calculated from those of the fuel and cladding evaluated at the outer fuel temperature and inner cladding temperature respectively

$$\lambda_{\text{eff}} = \frac{2\lambda_c \lambda_f}{\lambda_c + \lambda_f} . \tag{3.28}$$

The total pressure exerted by the mixture of gases contained in the fuel rod free volume is equal to the sum of partial pressures of each component. Its value changes in response to the combined effects produced by the following processes:

- Fission gas release - increasing the number of xenon atoms in the gas.
- Fuel swelling - decreasing the volume occupied by gas.
- Fuel and cladding thermal expansion - decreasing the volume occupied by gas.
- Temperature changes under transient conditions - affecting the temperature of the gas.

BELLA updates the total pressure of the helium-xenon mixture at every simulation time step based on the ideal gas law

$$P = P_{\text{He}} + P_{\text{Xe}} = (N_{\text{He}} + N_{\text{Xe}}) N_A \frac{\Re T_g}{V} , \tag{3.29}$$

where $T_g = (T_{out}^f + T_{in}^c)/2$ is the average temperature of the fuel-cladding gap. The above expression is used regardless of the existence of such a gap. However, it is important to note that while it is completely closed, the volume available is limited to the plenum above the fuel pellet column. Detailed analysis and quantification of the radial stresses induced by swelling and thermal expansion at the fuel-cladding interface are beyond the scope of this thesis. Therefore, BELLA approximates the interface pressure stated in eq. (3.26) by the total pressure of the gas mixture P.

4 Results from simulation of SEALER

The performance of SEALER during UTOP was simulated using BELLA. Rather than providing a detailed description of the phenomena involved during the transient and their impact on the main parameters of the primary system, the focus of this chapter is on the differences introduced by the new thermo-mechanical module as compared to the results obtained with the reference BELLA code. For further information on the the latter, see references Bortot et al. (2015) and Mickus et al. (2017). Recall that UTOP stands for Unprotected Transient Over-Power, meaning that all shut-down assemblies fail to insert. Under this assumption, SEALER relies entirely on negative reactivity feedback coefficients to achieve sub-criticality. Finally, the heat transfer from the primary to the secondary system is modelled in a simplified manner by imposing a constant temperature drop over the steam generators.

The UTOP was simulated for an external reactivity insertion of 0.5 $ over a time interval of one second at $t = 100$ s. In the case of SEALER, such insertion of positive reactivity is equivalent to the effect caused by the spurious withdrawal of a single control assembly at BOL (Wallenius et al., 2018). Prior to the onset of the transient, the reactor operates at full power under steady-state conditions. As a result of the reactivity insertion, the reactor moves towards super-criticality and the power level increases rapidly. Reactivity feedbacks arising from the fuel, that is, Doppler broadening and fuel axial expansion, cause an immediate response due to the fact that fuel temperatures rise almost instantaneously following the power excursion. On the other hand, the response time of the coolant temperature feedback is governed by the speed of sound in liquid lead, which is about 1800 m/s. Finally, the time for heat to be transferred to the coolant at the inlet of the core is usually of the order of hundreds of seconds, thus the diagrid radial expansion feedback shows a larger delay as compared to the other mechanisms. Once the combined negative reactivity introduced by fuel and coolant feedbacks balances out the initial insertion, the power level reaches a maximum and subsequently decreases.

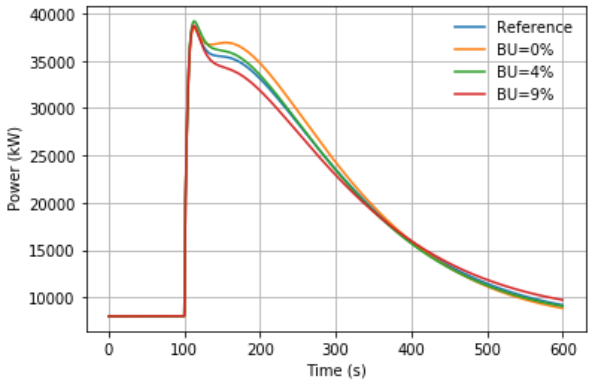

Figure 13: Thermal power level.

Neutronic parameters, that is, kinetic parameters and reactivity feedback coefficients, were previously calculated with Serpent for BOL conditions (Wallenius et al., 2018) and later manually introduced into the BELLA input file. It is important to note that simulations performed at different burnup steps used the same neutronic parameters. With this information, the discrepancy among the curves plotted in Figure 13 and Figure 14 must come from the influence of burnup on fuel and coolant temperatures. The negative reactivity introduced by Doppler

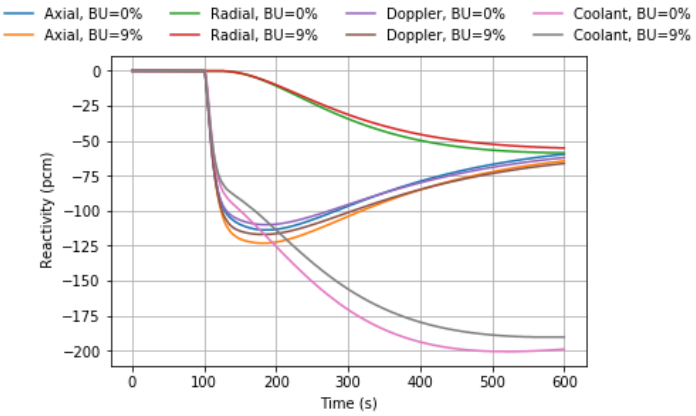

Figure 14: Reactivity feedbacks.

broadening and fuel axial expansion have a greater impact at high burnup, which indicates a higher average fuel temperature as compared to BOL conditions. On the contrary, the contribution from the coolant temperature feedback becomes more important at low burnup, meaning that the average core coolant temperature must decrease with increasing burnup.

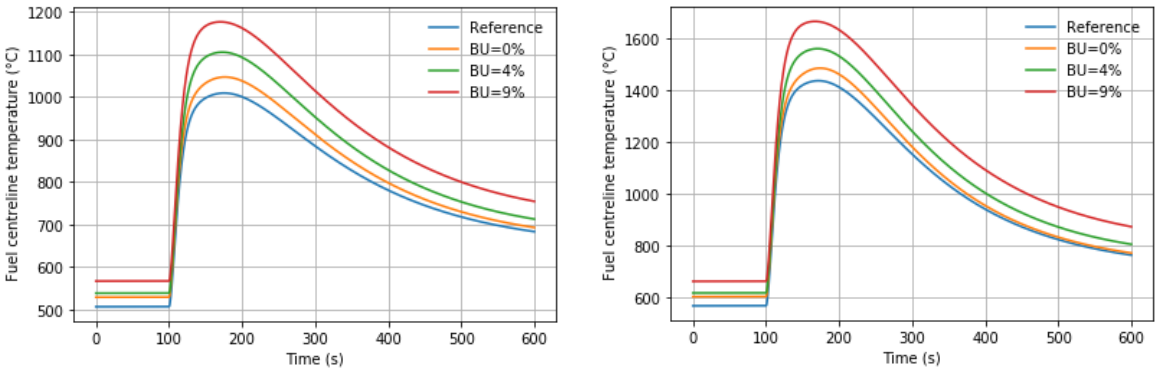

(a) Core average

(b) Peak assembly

Figure 15: Fuel centreline temperature.

The time evolution of the fuel centreline temperature is shown in Figure 15. Results are also shown for the peak assembly. First, the curve obtained using the reference BELLA code lies clearly below the rest. Nevertheless, the margin to fuel melting (2847 ºC) is still significant, as the maximum temperature is calculated at 1660 ºC. Secondly, both steady-state and transient temperatures reach higher values as burnup advances towards the EOL. Regarding the central region of the fuel, the predominant feature introduced by the new thermo-mechanical model is the improved expression for its thermal conductivity, which includes the detrimental effects of porosity, fission products and radiation damage (Figure 16). Since the degree of porosity is approximated solely by the fabricated porosity, its impact on thermal conductivity is independent of burnup and can be described by a constant factor. Therefore, it does not make any difference among the results obtained with the new BELLA code. However, the continuous formation of fission products entails a progressive reduction of the heat transfer rate from the central to the middle region of the fuel. Then, if energy balance equations are to be fulfilled under steady-state conditions, the fuel centreline temperature must increase as the

reactor moves towards EOL. This trend is further enhanced due to the stronger negative effect of radiation damage on thermal conductivity at higher temperatures. The reference BELLA code does not take into consideration any of the above effects. Consequently, the thermal conductivity of unirradiated, 100% dense, oxide fuel is the highest, resulting in the lowest fuel centreline temperature.

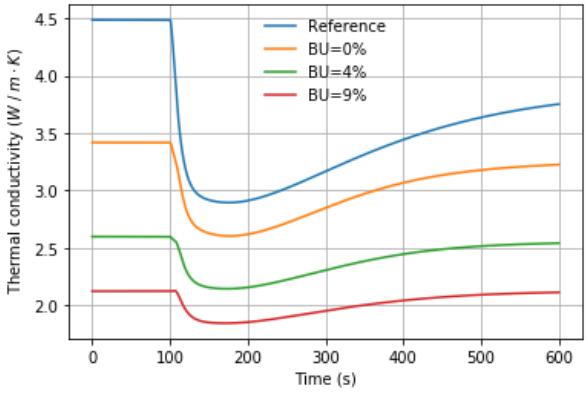

Figure 16: Fuel central region thermal conductivity.

Figure 17 shows the fuel outer temperature. In this case, discrepancies with respect to the reference BELLA code are motivated by several phenomena. Following the onset of the UTOP, the curve obtained under BOL conditions lies below the reference results due to the thermal expansion of the fuel along the radial direction. Despite the fact that the cladding also undergoes a net thermal expansion, the magnitude of the former is always greater because of exposure to much higher temperatures, thus leading to a decrease in the fuel-cladding gap thickness at the beginning of the transient (Figure 18). Then, recalling the effective heat transfer coefficient across an open gap defined in eq. (2.11), a reduction in thickness entails an improved heat transfer from fuel to cladding, which translates into a lower fuel outer temperature and a higher cladding inner temperature. Prior to the onset of the UTOP, under steady-state conditions, neither the fuel nor the cladding undergo thermal expansion because their temperatures remain constant. It is for this reason that the fuel outer temperature at BOL coincides to a large extent with the the reference results, only differing due to the relatively mild effect of porosity on thermal conductivity.

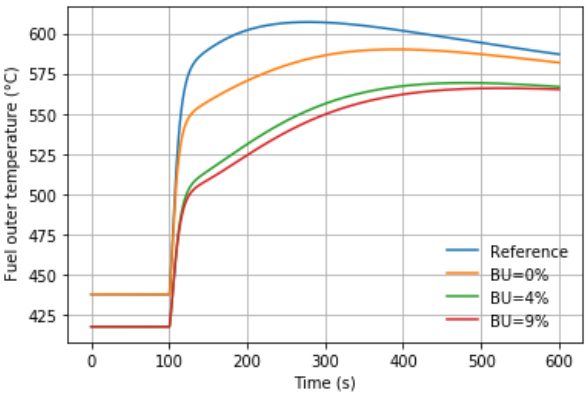

Figure 17: Fuel outer temperature.

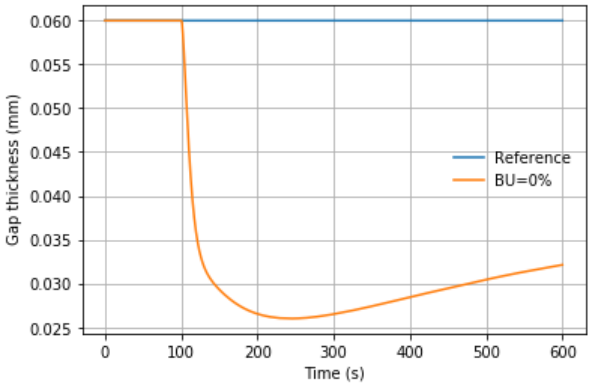

Figure 18: Fuel-cladding gap thickness under BOL conditions.

Given the design parameters of SEALER, the approach to modelling fuel swelling included in the new thermo-mechanical model predicts gap closure to occur around 3% burnup. Beyond such threshold, the gap remains closed throughout the entire transient calculation. Note that gap closure could also happen at lower burnup due to the thermal expansion of the fuel under transient conditions. In any case, fuel and cladding are in direct thermal contact while the gap remains closed. The solid-to-solid heat transfer coefficient is several orders of magnitude larger as compared to that of a gas-filled gap. Therefore, the rate of heat flow between the outer surface of the fuel and the inner wall of the cladding effectively becomes infinite when in contact. Then, the outer region of the fuel follows the same temperature evolution as the cladding inner region (Figure 19), hence its significantly lower value in comparison with the reference results.

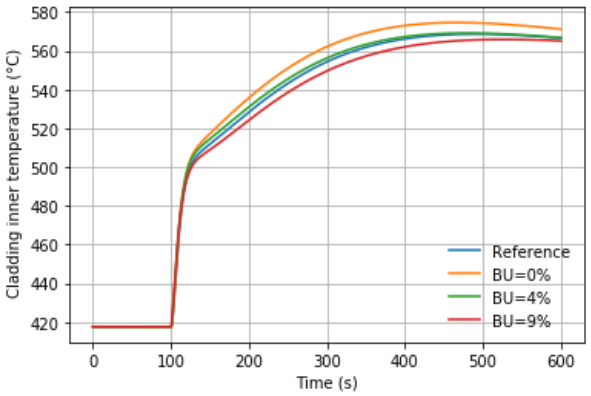

Figure 19: Cladding inner temperature.

Figure 17 shows yet another interesting feature which results from the implementation of the new thermo-mechanical module. As burnup advances beyond the above mentioned threshold, meaning that gap closure due to fuel swelling has already occurred, the fuel outer temperature reaches lower values throughout the transient. This indicates an improved heat transfer to the inner wall of the cladding. In order to understand the underlying reason it is convenient to recall the variables that influence the solid-to-solid heat transfer coefficient as defined in eq. (3.26). For that matter, the evolution of the fuel-cladding interface pressure, which BELLA approximates by the total pressure of the He-Xe has mixture, is plotted in Figure 20.

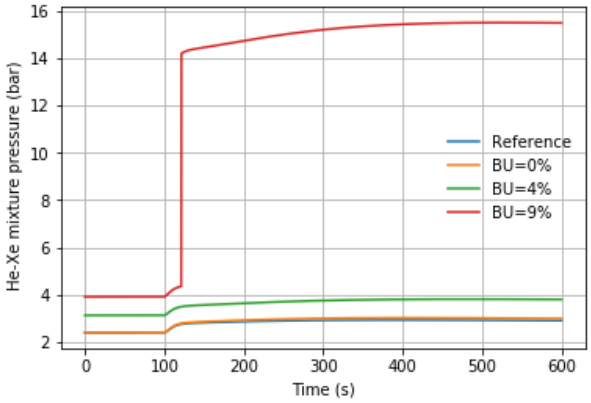

Figure 20: He-Xe mixture pressure.

Under steady-state conditions, higher burnup yields a higher pressure due to the combined effects of higher temperature operation and having a larger amount of xenon atoms in the gap. Shortly after the onset of the UTOP, the temperature of the gas mixture increases, hence its pressure. As for the simulation performed at 9% burnup, results also show a very steep jump of nearly 10 bar within the first 25 seconds of transient. Such a sudden increase in pressure suggests that at least one region of the fuel reached the Vitanza threshold, presumably the central region as it is exposed to the highest temperatures, releasing its gaseous xenon content. Fission gas release into the free volume of the fuel rod and subsequent pressure build-up enhances heat conduction from the fuel to the cladding, thus the higher outer temperature of the fuel at 4% than at 9% burnup.

The previous statement is valid provided that the gap remains closed. In this context, fission gases are released into the gas plenum above the fuel column and heat transfer between the fuel and cladding is dominated by the pressure at the interface. However, it is important to note that at low burnup, where the gap is generally open, fission gas release has a negative impact on heat transfer. This is due to the fact that the effective thermal conductivity of the gas mixture decreases with increasing number of xenon atoms (Figure 11).

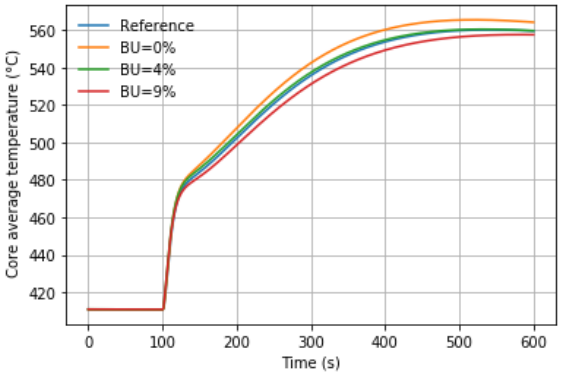

Figure 21: Core coolant average temperature.

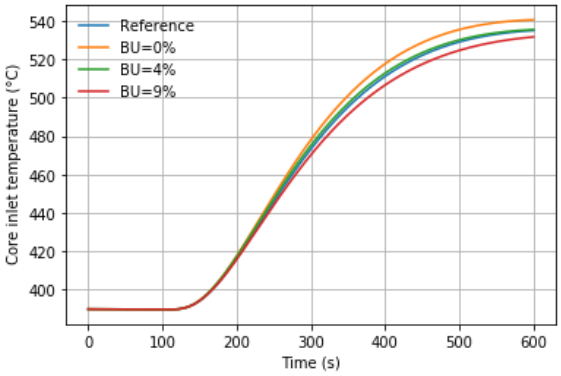

Figure 22: Core coolant inlet temperature.

Core average and inlet temperatures are plotted to justify the differences in coolant reactivity feedbacks observed in Figure 14. Both variables reach higher values at lower burnup,

thus coolant temperature and diagrid radial expansion feedbacks entail a larger reactivity insertion (in absolute terms) under BOL conditions. The order of magnitude of their respective response times can be qualitatively estimated from the plots. Finally, the fuel average temperature evolution is shown in Figure 23. As expected, results show that EOL conditions entail a higher average fuel temperature relative to BOL, meaning a larger insertion of negative reactivity following the sudden power level increase.

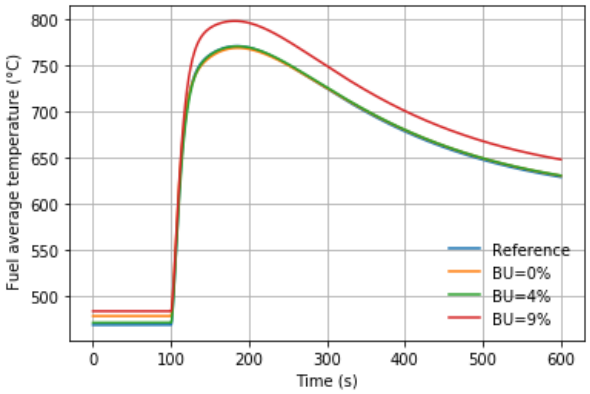

Figure 23: Fuel average temperature.

5 Environmental impact

The environmental impact caused as a result of the research developed in this thesis is relatively small. The entire work consisted of literature review, development of physical models and their subsequent implementation in a computer code, thus requiring only a computer with sufficient computing power. However, any engineering project carried out under the current Spanish legislation must be supported by an environmental assessment that ensures long-term sustainability and evaluates its possible negative impacts on the environment. On this basis, the carbon footprint of the project is calculated in this chapter.

The author's relocation from his residence in Barcelona to his new workplace in Stockholm is the single largest source of greenhouse gas emissions. Air transportation was chosen when travelling between the two destinations, separated by a distance of about 2300 km. Despite the fact that emissions per passenger and kilometer depend on several factors, a study from Chalmers University of Technology estimates an average emission factor of 163 gCO_2-eq/km per passenger in the case of economy scheduled flights (Larsson and Kamb, 2019). The author travelled the distance between Barcelona and Stockholm on two occasions (outbound and return flights), which results in a total travelled distance of 4600 km. With this information, the carbon footprint of the two trips combined adds up to approximately 750 $kgCO_2$-eq.

The carbon footprint of the computer hardware used to complete this thesis is also considered. It consisted of a HP Pavilion 14 laptop with an average power consumption under load of 62 W (Glaser, 2020) and a 24-inch LCD monitor. In view of the lack of information concerning the power consumption of the monitor, its value was estimated at 50 W. Assuming that the author made use of computer hardware during 8 hours per day for a total of 90 days yields an usage of 720 hours, thus an energy consumption of 80.6 kWh. Then, the CO_2 emissions derived from the consumption of such amount of energy in the form of electricity depends on the share of coal, oil and gas in the electricity generation mix of Sweden (Table 3).

Table 3: Electricity generation by energy source in Sweden during 2019. (International Energy Agency, 2019)

Source	**Generation (GWh)**	**Share (%)**	**Absolute emissions ($MtCO_2$)**	**Specific emissions ($kgCO_2$/kWh)**
Coal	1637	1.0	2.9	1.8
Oil	275	0.2	0.4	1.5
Natural gas	755	0.4	0.4	0.5
Low-carbon	165749	98.4	0.0	0.0

Finally, adding up the specific emissions presented for each source and multiplying the resulting quantity by the energy consumption calculated previously yields a value of 1.8 $kgCO_2$. Since the carbon footprint of the computer hardware is two orders of magnitude lower as compared to flying, it is concluded that the environmental impact of this thesis is mainly due to the emission of 750 $kgCO_2$-eq from air transportation.

6 Expenses

This chapter is devoted to estimating the cost of the resources that were spent on the realization of this thesis. Expenses are classified into three categories according to their origin: human resources, computer hardware, and energy consumption. In the case of tangible resources, that is, computer hardware, a linear depreciation method is used to distribute their acquisition cost over their estimated lifespan. Then, the reduction in the value of such items that occurs over time due to usage is calculated as

$$\text{Depreciation} = \frac{\text{Acquisition cost}}{\text{Lifespan}} \cdot \text{Usage} \,. \tag{6.1}$$

Note that lifespan in Table 4 is expressed in full-years, whereas in the above equation its value must be input in terms of working hours for consistency with the units employed for the usage. To that end, it is assumed that there are 250 working days within a full-year, each containing 8 working hours.

Table 4: Depreciation expenses of computer hardware.

Computer hardware	**Acquisition cost (€)**	**Lifespan (yr*)**	**Usage (h)**	**Depreciation (€)**
HP Pavilion 14 laptop	700	6	720	42.0
24-inch LCD monitor	130	10	720	0.5

(*) Full-year.

Table 5: Project costs.

Description		**Unit price**	**Unit**	**Number**	**Total price**
1. Human resources					
1.1	Research engineer salary	16.84 €	h	720	12,122.06 €
1.2	Travel expenses	95.00 €	u	2	190.00 €
	Subtotal				**12,312.06 €**
2. Computer hardware					
2.1	HP Pavilion 14 laptop	42.00 €	u	1	42.00 €
2.2	24-inch LCD monitor	0.52 €	u	1	0.52 €
	Subtotal				**42.52 €**
3. Energy consumption					
3.1	Electricity consumption	0.18 €	kWh	80.6	14.72 €
	Subtotal				**14.72 €**
Gross total cost					12,369.30 €
V.A.T. (25 %)					3,092.33 €
Net total cost					**15,461.63 €**

Conclusions

The most important physical processes affecting fuel properties and behaviour were modelled and integrated into the reference BELLA code, enabling a more accurate description of the thermo-mechanical evolution of the fuel and cladding under steady-state and transient conditions. The phenomena contemplated in the model arise from the combined effects of temperature variations, fission product formation, and radiation damage on the crystal structure of the oxide fuel. The main reason for developing and implementing fuel thermo-mechanics in the reference BELLA code is to asses the impact of microstructural transformations on key reactor design parameters, such as thermal conductivity of the fuel and thickness of the fuel-cladding gap.

The performance of SEALER-Artic under UTOP conditions was simulated using BELLA with and without the fuel thermo-mechanics extension at three different burnup steps, representative of beginning, middle and end of life conditions. The results indicate that the fuel centreline temperature is underestimated by the reference code, and that higher values are reached as burnup increases due to the detrimental effect of fission products and irradiation on thermal conductivity. Nevertheless, the margin to fuel melting (2847 ºC) is still significant, since the maximum fuel centreline temperature following the positive reactivity insertion is 1660 ºC. Conversely, the fuel outer temperature is overestimated. There are essentially two reasons for this, depending on the burnup. Under BOL conditions, the thickness of the gap decreases due to the thermal expansion of the fuel, thereby enhancing heat transfer from the fuel to the cladding. On the other hand, as burnup increases beyond 3%, gap closure occurs and direct solid-to-solid contact yields a much better heat conduction than a helium-filled gap.

The fact that gap closing is predicted at such a low burnup was unexpected and might motivate a future revision of the fuel rod design, as stress corrosion cracking may eventually degrade the structural integrity of the cladding in case of prolonged fuel-cladding mechanical interaction. Future work includes a benchmark analysis of the new thermo-mechanical model with respect to a qualified system code, for instance, SAS4A/SASSYS-1 (SAS), and a more detailed assessment of the internal stresses arising in the fuel pellet from the differential thermal expansion and at the fuel-cladding interface from the swelling of the fuel.

Acknowledgements

Foremost, I would like to express my sincere gratitude to my supervisor Prof. Janne Wallenius for offering me the opportunity to contribute my tiny share to the development of SEALER and providing guidance and feedback throughout the process. It has truly been a pleasure working with you. I would also like to acknowledge Ignas Mickus as the second reader of this thesis, and I am deeply grateful for his very valuable comments.

Secondly, I am using this opportunity to thank the people who I have come across during my master's degree at Universitat Politècnica de Catalunya. On the one hand, to all its teachers for their dedication and invaluable knowledge, especially Profs. Lluís Batet, Jordi Freixa, and Daniel Suarez, with whom I spent countless hours in Zoom during the spring semester. And on the other hand, to my dear classmates Krzysztof, Mario, and Narcís. It has been an immense pleasure to walk this path with you and I truly hope that our professional paths will cross again in the future (*See you at the top!*). In the meantime, we will always have our friendship that was based on so many good moments, both professionally and personally.

Last but not least, I would like to thank my parents and my brother Miquel for their unparalleled love and unconditional support. Us estimo molt!

References

American Nuclear Society. (1994). American National Standard for Decay Heat Power in Light Water Reactors.

Bailly, H., Menessier, D., & Prunier, C. (1999). *The nuclear fuel of pressurized water reactors and fast reactors: Design and behaviour*. Commissariat a l'Energie Atomique.

Blasius, H. (1913). Das Aehnlichkeitsgesetz bei Reibungsvorgängen in Flüssigkeiten. *Verein deutscher Ingenieure*, *131*, 1–41. https://doi.org/https://doi.org/10.1007/978-3-662-02239-9_1

Bortot, S., Suvdantsetseg, E., & Wallenius, J. (2015). BELLA: A multi-point dynamics code for safety-informed design of fast reactors. *Annals of Nuclear Energy*, *85*, 228–235. https://doi.org/10.1016/j.anucene.2015.05.017

Cahalan, J., Dunn, F., Herzog, J., White, A., & Wigeland, R. (2012). The SAS4A / SASSYS Safety Analysis Code System.

Carelli, M. D., Garrone, P., Locatelli, G., Mancini, M., Mycoff, C., Trucco, P., & Ricotti, M. E. (2010). Economic features of integral, modular, small-to-medium size reactors. *Progress in Nuclear Energy*, *52*(4), 403–414. https://doi.org/10.1016/j.pnucene.2009.09.003

Duriez, C., Alessandri, J., Gervais, T., & Philipponneau, Y. (2000). Thermal conductivity of hypostoichiometric low Pu content (U,Pu)O_{2-x} mixed oxide. *Journal of Nuclear Materials*, *277*(2-3), 143–158. https://doi.org/10.1016/S0022-3115(99)00205-6

Glaser, F. (2020). *HP Pavilion 14 Laptop Review*. Retrieved January 9, 2021, from https://www.notebookcheck.net/HP-Pavilion-14-Laptop-Review-A-stylish-all-rounder-with-a-bright-display.450936.0.html

IAEA. (2020). *Advances in Small Modular Reactor Technology Developments. A Supplement to: IAEA Advanced Reactors Information System (ARIS)* (tech. rep.).

Idelchik, I. (1966). *Handbook of Hydraulic Resistance: Coefficients of Local Resistance and of Friction* (Israel Program for Scientific Translations Ltd.).

International Energy Agency. (2019). *Energy Transitions Indicators* (tech. rep.). https://www.iea.org/reports/energy-transitions-indicators

Larsson, J., & Kamb, A. (2019). *Travel and climate: Methodology Report. Version 2.0* (tech. rep.). Chalmers University of Technology, Department of Space, Earth and Environment.

Lassmann, K., & Pazdera, F. (1983). URGAP: a gap conductance model for transient conditions. *Specialists' meeting on fuel element performance computer modelling.*, 97–113.

Lewis, C., MacSweeney, R., Kirschel, M., Josten, W., Roulstone, T., & Locatelli, G. (2016). *Small modular reactors: Can building nuclear power become more cost-effective?*

Lokhov, A., Sozoniuk, V., & Rothwell, G. (2016). Small Modular Reactors: Nuclear Energy Market Potential for Near-term Deployment. *Nuclear Development 2016*. https://www.oecd-nea.org/ndd/pubs/2016/7213-smrs.pdf

Lovering, J. R., Yip, A., & Nordhaus, T. (2016). Historical construction costs of global nuclear power reactors. *Energy Policy*, *91*, 371–382. https://doi.org/10.1016/j.enpol.2016.01.011

Lucuta, P., Matzke, H., & Hastings, I. (1996). UO_2 fuel : Review and recommendations. *Journal of Nuclear Materials*, *3115*(96), 166–180.

Mickus, I., Wallenius, J., & Bortot, S. (2017). Preliminary Transient Analysis of SEALER. *IAEA-CN245-433*, 1–10.

Mikityuk, K. (2009). Heat transfer to liquid metal: Review of data and correlations for tube bundles. *Nuclear Engineering and Design*, *239*(4), 680–687. https://doi.org/10.1016/j.nucengdes.2008.12.014

NEA. (2020). *Unlocking Reductions in the Construction Costs of Nuclear: A Practical Guide for Stakeholders* (tech. rep.). https://doi.org/10.1787/33ba86e1-en

Pascard, R. (1985). Les combustibles nucléaires céramiques. *Annales de Chimie Françaises*, *10*.

Paulsen, M. P., Peterson, C. E., Gose, G. C., Shatford, J. G., Westacott, J. L., & Kadakia, H. J. (2014). *RETRAN-3D – A Program for Transient Thermal-Hydraulic Analysis of Complex Fluid Flow Systems, Volume 1: Theory and Numerics*. https://www.epri.com/research/products/NP-7450-V3R3

Ronchi, C., Sheindlin, M., Musella, M., & Hyland, G. (1999). Thermal Conductivity of Uranium Dioxide up to 2900 K from Simultaneous Measurement of the Heat Capacity and Thermal Diffusivity. *Journal of Applied Physics*, *85*(2), 776–789.

Seban, R., & Shimazaki, T. (1951). Heat transfer to a fluid flowing turbulently in a smooth pipe with wall at constant temperature. *Transactions of the ASME*, *73*, 803–809. https://www.osti.gov/biblio/4404784

Tourasse, M., Boidron, M., & Pasquet, B. (1992). Fission product behaviour in PHENIX fuel pins at high burnup. *Journal of Nuclear Materials*, *188*, 49–57. https://doi.org/https://doi.org/10.1016/0022-3115(92)90453-R

University of Chicago. (2004). The Economic Future of Nuclear Power.

Van Uffelen, P. (2006). Modelling of Nuclear Fuel Behaviour. *Frédéric Joliot & Otto Hahn Summer School on Nuclear Reactors - Physics, Fuels and Systems*.

Wallenius, J., Qvist, S., Mickus, I., Bortot, S., Szakalos, P., & Ejenstam, J. (2018). Design of SEALER, a very small lead-cooled reactor for commercial power production in off-grid applications. *Nuclear Engineering and Design*, *338*, 23–33. https://doi.org/10.1016/j.nucengdes.2018.07.031

Wallenius, J., Qvist, S., Mickus, I., & Szakalos, P. (2019). SEALER-UK: a 55 MWe lead-cooled reactor for commercial power production. *Technical Meeting on the Benefits and Challenges of Fast Reactors of the SMR Type*.

Winter, P., & MacInnes, D. (1988). The thermal conductivity of UO_2. *Technical Committee Meeting on Water Reactor Fuel Element Computer Modelling in Steady-State, Transient and Accident Conditions*.

World Nuclear Association. (2017). *Nuclear Power Economics and Project Structuring - 2017 Edition* (tech. rep.).

Appendix A: Numerical methods

The composite Simpson's rule is used to evaluate the definite integrals that appear in the mathematical formulation of BELLA. The method consists of partitioning the integration domain $[a, b]$ into an even number of subintervals N of equal width

$$h = \frac{b-a}{N} \,, \tag{.2}$$

with endpoints at $\{x_0, ..., x_N\}$, then approximating the curve in each subinterval using a second-order polynomial. That said, the composite Simpson's rule is given by

$$\begin{aligned} \int_a^b f(x)dx &= \sum_{k=0}^{N/2-1} \int_{x_{2k}}^{x_{2k+2}} f(x)dx \\ &\simeq \frac{h}{3} \sum_{k=0}^{N/2-1} (f_{2k} + 4f_{2k+1} + f_{2k+2}) \\ &= \frac{h}{3} \left[f_0 + 4f_1 + 2f_2 + 4f_3 + 2f_4 + ... + 4f_{N-1} + f_N\right] \,, \end{aligned} \tag{.3}$$

where f_k denotes $f(x_k)$. The error in approximating an integral by this method is asymptotically proportional to h^4, which is considerably lower than that obtained with the Trapezoidal rule.

Appendix B: BELLA computer code

The current version of BELLA was developed in Python. The source code files, which can be found in the attached folder with the name `BELLA`, are presented in this appendix. Prior to launching a transient calculation, the user must define all the parameters stated in the input file appended below. In this case, it was specified to match the design parameters of SEALER-Arctic. Then, it only remains to execute the file `main.py` and select the desired execution options from those provided by BELLA's user interface. Note that the option `Post-process data set` does not function properly since it was originally coded to process the results obtained with a previous version of the code. At the end of every simulation, a text file is automatically generated containing the value of the main primary side variables at every simulation time step.

- `main.py` - Main execution file
- `pre.py` - Pre-processing module
- `ini.py` - Initialization module
- `solve.py` - Solver module
- `mprop.py` - Material properties module
- `post.py` - Not used
- `input_Arctic.inp` - Input file

The folder named `Output` contains the output files of the simulations carried out to evaluate the performance of SEALER-Arctic under UTOP conditions. Moreover, it includes the script `plot.py` used to plot the evolution of each primary side variable throughout the transient calculation.

- `plot.py` - Post-processing file
- `Reference` - UTOP results without thermo-mechanics extension
- `BU0` - UTOP results at 0% burnup
- `BU4` - UTOP results at 4% burnup
- `BU9` - UTOP results at 9% burnup

```
######################################################################
#                                                                    #
#                  BELLA 0.1.1. Input file                           #
#                        2020.12.16                                  #
#                                                                    #
#   - Comments are written starting line with #                      #
#   - No comments in data lines                                      #
#   - Variable sequence not important                                #
#   - Empty lines not important                                      #
#   - Input format is: variable_name value (separated by space)      #
#   - Variable unit indicated in [ ]                                 #
#   - No data stored during inactive time                            #
#   - ULOHS w decay heat: time_step <= 0.025                         #
#                                                                    #
######################################################################

######################################################################
#                       FUEL PARAMETERS                              #
######################################################################

# Burnup [at.%]
burnup 0.0
# Radial peaking factor [-]
rad_peak_factor 1.55
# Xenon fission yield [atoms/fiss]
xe_fiss_yield 0.23
# Xenon release-to-birth ratio below Vitanza threshold [-]
release_birth_xe 0.01
# Energy released per fission event [MeV]
fission_energy 200.0
# Fuel surface roughness [mm]
roughness_fuel 2.24e-3
# Cladding surface roughness [mm]
roughness_clad 1.78e-3

######################################################################
#                       HYDRAULIC PARAMETERS                         #
######################################################################

# Pump head decay constant [1/s]
pump_constant 20
# Foot inlet resistance coefficient [-]
resistance_coeff 1.5

######################################################################
#                       SYSTEM GEOMETRY                              #
######################################################################

###################### Core design parameters ######################
```

```
# Fuel assemblies [-]
assemblies_fuel 19
# Fuel pins per assembly [-]
pins_assembly 91
# Fuel pin pitch [mm]
pitch_pin 16.37

####################### Fuel pin design parameters #################
# Fuel pellet porosity [-]
porosity 0.04
# Fuel pellet diameter (hot) [mm]
diameter_fuel 13.4
# Cladding outer diameter (hot) [mm]
diameter_clad_out 14.52
# Cladding thickness [mm]
thickness_clad 0.5
# Fuel column height (hot) [mm]
height_fuel 1106.0
# Gas plenum height [mm]
height_gas_plenum 350.0
# Upper end cap height [mm]
height_upper_endcap 20.0
# Lower end cap height [mm]
height_lower_endcap 50.0
# Insulation pellet height [mm]
height_insulation 10.0
# Lower shield height [mm]
height_shield 50.0

####################### Fuel assembly duct design parameters #######
# Hex-can inner flat-to-flat [mm]
ftf_hexcan_in 160.0
# Hex-can thickness [mm]
thickness_duct 2.0
# Fuel assembly height [mm]
height_duct 1890.0
# Foot slot width [mm]
slot_width 20.0
# Foot slot height [mm]
slot_height 100.0
# Number of slots per assembly [-]
slot_number 8
# Foot inner radius [mm]
radius_foot_in 40.0
# Number of rails per assembly [-]
rail_number 19
# Rail width [mm]
rail_width 2.0
# Assembly head inner radius [mm]
```

```
radius_head_in 75.0
# Assembly grip width [mm]
grip_width 10.0

####################### Primary system design parameters ###########
# Core barrel inner diameter [mm]
diameter_barrel_in 1708.0
# Core barrel outer diameter [mm]
diameter_barrel_out 1748.0
# Primary vessel inner diameter [mm]
diameter_vessel_in 2648.0
# Primary vessel outer diameter [mm]
diameter_vessel_out 2748.0
# Vessel total height (w/o lit) [mm]
height_vessel 5600.0
# Number of steam generators [-]
no_sg 8
# Steam generator elevation (relative to core outlet) [mm]
elevation_sg 1210.0
# Cold pool volume [m3]
volume_coldpool 3.3

####################### Steam generator design parameters ##########
# Tubes per steam generator [-]
tubes_sg 10
# Tube inner diameter [mm]
diameter_sgtube_in 16.0
# Tube outer diameter [mm]
diameter_sgtube_out 20.0
# Tube pitch [mm]
pitch_sgtube 23.5
# Spiral initial radius [mm]
radius_sgstack_in 110.0
# Spiral terminal radius [mm]
radius_sgstack_out 194.0
# Steam generator height [mm]
height_sg 300.0

#########################################################################
#                      RADIATIVE HEAT TRANSFER                          #
#########################################################################

# Fuel thermal emissivity [-]
emissivity_fuel 0.9
# Cladding thermal emissivity [-]
emissivity_clad 0.8
# Primary vessel thermal emissivity [-]
emissivity_vessel 0.85
# Ambient emissivity [-]
```

```
emissivity_amb 0.2
# Ambient temperature [ºC]
temp_amb 20

######################################################################
#                       NEUTRONIC PARAMETERS                         #
######################################################################

####################### Reactivity coefficients ####################
# Doppler constant [pcm]
k_doppler -335.0
# Coolant density reactivity feedback coefficient [pcm/K]
alpha_pb -1.30
# Radial expansion reactivity feedback coefficient [pcm/K]
alpha_radial -0.39
# Axial expansion reactivity feedback coefficient [pcm/K]
alpha_axial -0.39

####################### Kinetic parameters ##########################
# Effective prompt neutron generation time [s]
neutron_gen_time 0.212e-6
# Delayed neutron fractions [pcm]
delayed_fraction_g1 11.1
delayed_fraction_g2 98.2
delayed_fraction_g3 81.1
delayed_fraction_g4 140.2
delayed_fraction_g5 198.0
delayed_fraction_g6 99.4
delayed_fraction_g7 65.0
delayed_fraction_g8 23.8
# Delayed neutron decay constants [s]
decay_rate_g1 0.0125
decay_rate_g2 0.0283
decay_rate_g3 0.0425
decay_rate_g4 0.133
decay_rate_g5 0.292
decay_rate_g6 0.666
decay_rate_g7 1.63
decay_rate_g8 3.55

######################################################################
#                       BALANCE OF PLANT PARAMETERS                  #
######################################################################

# Nominal power level [W]
power_core_ini 8e6
# Nominal core inlet temperature [ºC]
temp_pb_core_in 390.0
# Nominal temperature rise over the core [ºC]
```

```
deltaT_core_ini 42.0
# Lead free surface level at shut-down [mm]
level_pb_shut 4725.0

#########################################################################
#                       SIMULATION PARAMETERS                           #
#########################################################################

# Case 0 - Steady-state
# Case 1 - UTOP
# Case 2 - ULOF with constant dTsg
# Case 3 - ULOF with constant Psg
# Case 4 - ULOHS
# Case 8 - ULOHS and ULOF
# Case 9 - SCRAM
# Case 10 - Blocked assembly

# Transient case
transient_case 1
# Simulate x seconds of inactive time for convergence to initial steady-state
inactive_time 10.0
# Simulate x seconds of steady-state before initiating transient
ss_time 100.0
# Simulation end time [s]
sim_end_time 600.0
# Simulation time step [s]
time_step 0.025
# Neutronics calculation flag (1 yes 0 no)
calculate_neutronics 1
# Decay heat calculation flag (1 yes 0 no)
calculate_decay 1
# Thermal expansion calculation flag (1 yes 0 no)
calculate_expansion 1
# External reactivity (used in UTOP) [beta effective]
ext_reactivity 0.5
# Programmed reactivity (used in SCRAM) [pcm]
prog_reactivity -1000.0
```